Displacement of extracellular chloride by sulfated glycosaminoglycans of the brain's extracellular matrix

Kieran P Normoyle,[1,2] Kyle P Lillis,[1,2] Kiyoshi Egawa,[3] Melanie A McNally,[1,2] and Kevin J Staley[1,2]

1. Department of Neurology, Division of Child Neurology, Massachusetts General Hospital, Boston, MA, United States
2. Department of Neurology, Harvard Medical School, Boston, MA, United States
3. Department of Medicine, Hokaiddo University, Sapporo, Hokaiddo, Japan

Abstract

GABA is the primary inhibitory neurotransmitter. Membrane currents evoked by $GABA_A$ receptor activation have uniquely small driving forces: their reversal potential (E_{GABA}) is very close to the resting membrane potential. As a consequence, $GABA_A$ currents can flow in either direction, depending on both the membrane potential and the local intra and extracellular concentrations of the primary permeant ion, chloride (Cl). Local cytoplasmic Cl concentrations vary widely due to displacement of mobile Cl ions by relatively immobile anions. Here we describe new reporters of extracellular chloride (Cl^-_o) and demonstrate that Cl is displaced in the extracellular space by high and spatially heterogenous concentrations of sulfated glycosaminoglycans (sGAGs). Cl^-_o varies widely, and the mean Cl^-_o is only half the canonical concentration, i.e. the Cl concentration in the cerebrospinal fluid. Cl^-_o microdomains provide a mechanism to link the varied but highly stable distribution of sGAGs in the brain's extracellular space to neuronal signal processing via the effects on the amplitude and direction of $GABA_A$ transmembrane Cl currents.

Introduction

$GABA_A$ synapses comprise the primary output for inhibitory interneurons in the brain.[1, 2] A unique feature of $GABA_A$ synapses are the very small driving forces for ion flux through open $GABA_A$ receptor-operated membrane channels. The reversal potential for the primary permeant ion, chloride, is usually within a few mV of the neuronal resting membrane potential (RMP),[3] and may even be positive to RMP.[4, 5] This low driving force makes possible a novel form of synaptic plasticity at $GABA_A$ synapses: the direction of current flow, i.e. the effect of $GABA_A$ receptor activation on the resting membrane potential, can be reversed by low millimolar alterations in the local chloride concentration.[6] Such physiological variance is routinely observed in individual studies[7, 8] and is likely to underlie the 25 mV range of reported group mean reversal potentials in 20 recent studies of evoked $GABA_A$ currents recorded with gramicidin perforated patch electrodes in area CA1 of the hippocampus (tabulated in Rahmati et al. 2021).[9] This variance has substantial effects on synaptic signaling: the reversal potential of $GABA_A$ currents evoked in a single pyramidal cell by stimulation of 8 different presynaptic interneurons also varied by over 20 mV.[9]

We have proposed that the intracellular chloride concentration (Cl^-_i) is not monotonic across the neuronal cytoplasm, but rather varies inversely with the local concentration of macromolecular anions that comprise the vast majority of intracellular anions.[9, 10] This phenomenon is known as Donnan exclusion.[11-15] Mobile ions, in this case Cl, are repelled by relatively immobile ions such as proteins with negative surface charges. Many proteins such as gephyrin that are associated with $GABA_A$ synapses bear large negative surface charges,[16] suggesting that variance in the $GABA_A$ reversal potential (E_{GABA}) is determined by local fixed cytoplasmic charge densities. However, E_{GABA} is not determined solely by Cl^-_i but rather by the ratio of intra to extracellular permeant ions. This raises the possibility that spatial variance in the extracellular Cl concentration (Cl^-_o) could also be an important determinant of E_{GABA}.

The displacement of Cl^- by fixed negative charges should also occur in the extracellular space, where the high negative charge density of the polysulfated glycosaminoglycans (GAGs) that comprise the bulk of the extracellular matrix[17] can be as high as the Cl^- concentration in the CSF.[18-20] Thus some to all of the local Cl^-_o could be displaced, depending on the degree of GAG sulfation. Such displacement has been most clearly demonstrated in the matrix of cartilaginous tissue, where the negative charge density of the extracellular matrix can reach 400 meq / liter,[21] but dozens of mM of Cl^-_o are also displaced by sulfated GAGs in tissues such as skin.[22]

Many findings suggest that the brain Cl^-_o is lower than the canonical value. Xray emission spectroscopy of the extracellular space has demonstrated sulfate concentrations as high as 100 mM.[20] Astrocytic buffering of Cl^-_o[23] would not be necessary if Cl^-_o were indeed > 100 mM. The gating of Group II and III metabotropic glutamate receptors, kainate receptors, acid-sensing membrane ion channels, and the transport rate of the GlyT1 glycine transporter are all strongly modulated by Cl^-_o over the entire range of 1 - 100 mM.[24-29] Such strong modulation by low Cl^-_o would not make sense if Cl^-_o was uniformly > 100 mM.

Studies of Cl^-_o are few, and have only been carried out with relatively large multibarreled ion-sensitive electrodes with tip diameters of 3-5 microns.[30] This technique creates a stab wound in the tissue that is surrounded by bulk extracellular fluid (containing no GAGs), that would have a

Cl^- concentration that is close to that of the perfusate. Modern Cl-selective microelectrodes are less damaging, and those studies demonstrate variance in Cl^-_o, but of only a few mM.[31]

A fluorometric study of Cl^-_o would provide a noninvasive means to establish the distribution of chloride in the extracellular space. However, no suitable Cl-sensitive organic fluorophores exist, and transgenic fluorophores such as SuperClomeleon[32] and CloPhensor[33] are not distributed in the extracellular space. We therefore developed a chloride-sensitive fluorophore from previously described organic backbones[34, 35] that satisfied the following criteria. First, the fluorophore should be sensitive to Cl in the range of the extracellular chloride concentration i.e. up to 100 mM; available fluorophores have been optimized for the low millimolar chloride concentrations of the cytoplasm. Second, the fluorophore should report Cl independently of the concentration of fluorophore. Ratiometric fluorophores suitable for the extracellular space do not exist, so we used **F**luorescence **L**ifetime **Im**aging (FLIM)[36] to remove the dependence of the fluorescence emission on fluorophore concentration. Third, the fluorophore should be constrained to the extracellular space, for which dextran conjugation is optimal.[37, 38] Fourth, the fluorophore should be excited by wavelengths that are not damaging to brain tissue, i.e. below the ultraviolet range and in the visible or infrared range. Fifth, many Cl sensors are also sensitive to pH,[39, 40] so a pH-insensitive fluorophore would be ideal. Finally, the fluorophore needs to be sufficiently bright so that its emission can be reliably distinguished from autofluorescence.

Here, we describe: a newly synthesized Cl-sensitive fluorophore that meets these 6 criteria; the demonstration of stable Donnan exclusion of chloride by sulfates fixed to GAG-like carbohydrate polymers; the demonstration that the Cl^-_o of *in vitro* and *in vivo* brain tissue is much lower than cerebrospinal or plasma chloride; a remarkable spatial variance in Cl^-_o (i.e. Cl^-_o microdomains); finally, as evidence that Cl^-_o is determined by Donnan exclusion of Cl by sulfated GAGs, we demonstrate that release of these sulfates by exogenous chondroitinase results in an increase in Cl^-_o.

Results

Non-invasive measurement of extracellular chloride using ABP-dextran: ABP is a novel Cl-sensitive fluorophore compatible with Fluorescence Lifetime IMaging (FLIM) that we have optimized to be bright, red-shifted, and sensitive to chloride concentrations through the range that would be encountered in in the extracellular space. We conjugated ABP to a 10,000 Dalton (10KDa) dextran resulting in an amine-bonded moiety that is resistant to pH changes in the physiological range and is restricted to the extracellular space (Figure 1A & S2). We validated the ability of ABP-dextran to reliably report chloride concentration by correlating the shortening of ABP-dextran fluorescence lifetime to chloride concentration (Figure 1B) through the Stern-Volmer relationship (Figure 1C), generating a k_{SV} of 19.3 mM. The emission lifetime of ABP-dextran is not dependent upon the concentration of ABP-dextran, only the concentration of chloride. Chloride concentration also affects ABP-dextran intensity, such that high chloride concentrations not only shorten the emission lifetime but also reduce the intensity of emission. However, the concentration of chloride can be calculated (independently of the local ABP-dextran concentration) as long as sufficient photons are collected to calculate fluorescence lifetime in a given pixel.

Sulfated agarose gels as an *in vitro* model of perineuronal space: We recently observed that differing concentrations of chloride juxtaposed to one another were stable on time scales of at

least 100 minutes due to the presence of immobile anionic charges present in the neuronal cytoplasm,[9] an effect known as Donnan exclusion.[12-15, 41] We tested whether Donnan exclusion was also operative in the extracellular space as a consequence of the fixed negative charges on the sulfate moieties of the glycosaminoglycans that comprise the bulk of the extracellular matrix.[17] This matrix is most frequently visualized as the perineuronal lattice-like structures found around all neurons and first described by Golgi in 1898.[42, 43] The process of Donnan exclusion does not require the input of energy, although this issue has been contested.[44, 45] We therefore modeled the brain's extracellular matrix using a reduced system to remove the possibility of active buffering of Cl^-_o by astrocytes[23] or other cellular elements. We used gels of sulfated agarose to mimic the sulfated glycosaminoglycans such as the chondroitin sulfate-decorated aggrecan family members that are prominent in the perineuronal matrix. Agarose is a nominally sulfate-free linear glycopolymer that is a major component of agar (Figure 2B; bars 1 and 2) that was used as a chemically homogenous starting material for covalent sulfate linkage. We optimized the method of Fuse and Suzuki[46] to balance the gelatinizing properties of agarose with the dispersive, hydrophilic Donnan effects arising from incorporation of the charged sulfate groups.[12, 47] We obtained a sulfated agarose that could be used to cast gels with 50 mM effective sulfate concentration (Figure 2B, bar 3; see also S1) covalently linked to the polymerized agarose lattice. Gels cast from sulfated agarose serve as a simple *in vitro* model of the perineuronal extracellular space, allowing us to investigate the ability of covalently linked anions attached to a three-dimensional matrix to displace mobile chloride ions.

When we measured the chloride concentration within non-sulfated agarose gels equilibrated in aCSF, we found no significant difference versus the perfusate aCSF (Figure 2C, left pair vs center pair) measured either with a standard colorimetric iron(III) thiocyanate assay (Figure 2C, light blue bars) or ABP-dextran FLIM imaging (Figure 2C, dark blue bars). Agarose gels with fixed anions in the form of covalently bound sulfate had significantly decreased chloride concentrations versus control aCSF or native agarose gels that had no fixed anions (Figure 2C, right pair vs center pair and left pair, respectively). Both assay methods, FLIM and iron thiocyanate, produced equivalent results in each material (Figure 2C, light blue bar on left vs dark blue bar on right of each pair). Next we placed separately cast non-sulfated and sulfated gels adjacent to each other and equilibrated in the same aCSF bath with ABP-dextran (Figure 2D; schematic in Figure 2A). ABP-dextran FLIM measurements of chloride concentration within the non-sulfated and sulfated gels demonstrated significant chloride concentration differences between gels that had no fixed anionic charge to displace mobile chloride (non-sulfated agarose; Figure 2D light blue bars) vs. gels that had covalently bound sulfate groups (sulfated agarose; Figure 2D dark blue bars). The Cl concentrations were inversely proportional to the sulfate concentration in the gel, and were stable for over three weeks. These findings support the displacement of mobile chloride ions by the sulfates fixed to the gel (Figure 2D) by Donnan exclusion. Finally, we imaged both non-sulfated and sulfated gels immediately juxtaposed to one another, along with aCSF perfusate, in the same field (Figure 2E) and demonstrated that the presence of sulfate groups covalently bound within the polymerized gel results in a significantly decreased chloride concentration relative to both non-sulfated gels and aCSF perfusate (Figure 2E, bar 3 vs bar 2 and bar 1, respectively).

<u>Demonstration of chloride displacement in living systems:</u> To test whether Donnan exclusion is also operative in the extracellular matrix of the brain, we studied mouse hippocampal organotypic slice cultures. We tested whether extracellular perineuronal fixed anions, such as the chondroitin sulfate moieties of aggrecan family proteoglycans,[17, 48] displace chloride in this

living system. After incubation with ABP-dextran and equilibration with aCSF containing ABP-dextran and 136mM chloride, we measured extracellular chloride concentration using ABP-dextran FLIM and found that Cl^-_o was unexpectedly low and heterogenous (46.7 +/- 18.8 mM, calculated from 25.8E6 pixels across 32 fields of 7 slices). Representative fields are shown in Figure 3A&B (ABP-dextran intensity images of low- and high-magnification, respectively) and Figure 3C (Cl^-_o composite image of high-magnification field, quantified in Figure 3D; see also Figure S4).

Perineuronal traces along the outer circumference of neuronal silhouettes (Figure 3C, white dashes) were used to analyze the spatial change in Cl^-_o in the extracellular space immediately adjacent to the neuronal cytoplasmic membrane (Figure 3E). We compared the size of the effects of fixed anions on local Cl^-_o to Brownian and machine noise arising from FLIM of ABP-dextran in bulk solutions with similar mean Cl^-_o. The pixel-to-pixel change in Cl^-_o (ΔCl^-_o) versus distance in the presence of fixed anions in the perineuronal space (Figure 3E, blue) was much larger than the ΔCl^-_o versus distance in the absence of fixed anions in bulk solution containing the same concentration of Cl^- and ABP-dextran (Figure 3E, red). Figure 3F shows similar data for a larger cohort of perineuronal tracings and their corresponding aCSF solution counterparts (N = 72). We found a consistently increased probability of greater ΔCl^-_o per micron in the extracellular space where fixed extracellular anions were present compared to the perfusate aCSF (Figure 3F, blue vs red). We further analyzed our data for extracellular microdomains of homogenous Cl^-_o and found that 90% of regions of similar Cl^-_o were 0.205μm^2 area (Figure S6-A), the smallest domain size we could resolve. The diffraction limits of light microscopy constrained the assessment of extracellular chloride microdomains much smaller than 0.2 um^2. There were no characteristic values of Cl^-_o associated with the most common sizes of extracellular microdomains (Figure S5-B).

We then confirmed that fixed anions, including chondroitin sulfate glycoproteins, are a significant contributor to this difference by measuring Cl^-_o before and after treatment with chondroitinase. Analogous to matrix metalloproteases, chondroitinase is a bacterial enzyme that cleaves the sulfated glycopolymer chondroitin. Chondroitinase treatment significantly increased Cl^-_o in organotypic hippocampal slice cultures (Figure 4A&B; pre- and post-digestion, respectively). Cl^-_o increased on average 8.3+/-3.3mM in freely diffusible extracellular chloride within the slice culture (Figure 4A vs 4B; quantified in 4D-F) and was significantly greater in chondroitinase digested slices than in sham digested slices (Figure 4B vs 4C; quantified in 4F). This increase in Cl^-_o coincides with a significant decrease in the extracellular fixed anions within the slice culture. The decrease in fixed anions in the extracellular space was estimated from the concentration of polysulfated chondroitin released into the perfusate after chondroitinase treatment (Figure 4G) and confirmed by HPLC analysis (Figure 4H). These observations are consistent with the inverse relationship between fixed extracellular anions and mobile Cl^-_o arising from Donnan exclusion. In summary, the immobile ions associated with the extracellular matrix displace mobile anions such as chloride, so that Cl^-_o is much lower and less uniform than expected.

<u>Chloride displacement in the perineuronal space *in vivo*</u>: To test whether Donnan exclusion of Cl^-_o by sulfated GAGs was significant *in vivo*, we performed live 2 photon imaging of P26-30 mice via a cortical window. Direct application of high concentrations of ABP-dextran into the non-sulfated agarose overlying the neocortex (Figure 5B) resulted in a robust ABP fluorescence signal from the extracellular space of the brain parenchyma. Control measurements were

obtained from the agarose above the cortex, which had been brought up in aCSF (136mM Cl^-) and allowed to equilibrate with *in vivo* CSF. Notable exclusion of ABP-dextran fluorescence emission from blood vessels (Figure 5C & S5A) and cell bodies (Figure 5C & S5C) was observed. Regions of interest were defined using intensity images to provide structural information; an example composite image can be seen in Figure 5D (see also Figure S5). Cortical Cl^-_o was less than half the chloride concentration measured in the overlying agarose (48.1 +/- 17.0mM, calculated from 68 ROI and 4 animals, vs 135.4 +/- 5.0mM in agarose above cortex). Regional mean Cl^-_o values were approximately 45-55mM (Figure 5E) but there was notable spatial variation between regions and even within regions (Figure 5D), consistent with local Donnan exclusion of Cl^-_o by variably sulfated GAGs. Thus the chloride concentration is much lower than expected in the extracellular space of the neocortex and is spatially heterogenous, creating Cl^-_o microdomains.

Discussion

We demonstrate stable Donnan exclusion of chloride by fixed anions in a transport-free system of sulfated agar using FLIM of a novel fluorophore, ABP-dextran, and validate these measurements with direct chemical assays of sulfate and chloride. FLIM of ABP-dextran demonstrated that Cl^-_o in the brain is less than half the Cl concentration in the cerebrospinal fluid and plasma. This low Cl^-_o arises from Donnan exclusion of chloride by fixed sulfated glycosaminoglycans (sGAGs), because release of sGAGs by chondroitinase results in an increase in Cl^-_o that varies with the amount of sulfates released. The distribution of chloride in the extracellular space of the brain varies substantially at micrometer dimensions, creating extracellular chloride microdomains.

Limitations of this study

The finding that Cl^-_o is much lower than expected in the extracellular space of living brain tissue is based on FLIM of a new Cl-sensitive fluorophore, ABP-dextran. These results are in contrast to the higher values measured using ion sensitive electrodes.[30, 31] The ABP-dextran fluorophore is based on a validated structure[34, 49] and was calibrated against Cl, other anions, and direct chemical analysis of chloride concentrations in situ. ABP-dextran FLIM accurately reported Cl values in sulfated carbohydrate polymers (Figure 2), so it is unlikely that the sGAGs or other anions in the extracellular environment (Figure 1C) affected the accuracy of the ABP-dextran FLIM. ABP-dextran overcomes several barriers to accurate measurement of extracellular chloride, including sufficient sensitivity in the relevant range of chloride concentrations, competition with autofluorescence, and permeation into the cytoplasmic space, where lower chloride values would be encountered. ABP-dextran was clearly excluded from the intracellular space (Figure 3A; Figure 5; Figure S2) and was far brighter than autofluorescence at 760nm 2-photon excitation (Figure S3). We speculate that the difference between the fluorophore-based measures and the ion-sensitive electrode measures of Cl^-_o likely arise from distortion of the extracellular milieu created by the stab wound of the microelectrode such that the microelectrode measures chloride in fluid comprised primarily of bulk CSF rather than fluid in which Donnan exclusion is operative.

Stable Donnan exclusion

An important finding in this study is that Cl microdomains established by Donnan exclusion are stable for weeks, and do not require active transport to be maintained (Figure 2). This phenomenon is well-established in biophysics,[14, 15] but is more confusing in neuronal physiology

where membranes with time-varying ionic permeabilities and transporters create a more complex environment.[9, 44, 50, 51] A point of particular confusion is the role of active Cl transport vs. Donnan exclusion in maintaining a particular E_{GABA} in the face of GABA-gated Cl flux that alters the local Cl concentration. After a GABA-gated Cl influx, and re-establishment of local charge balance by cationic flux via voltage- and ligand-gated cation channels, the local cytoplasm will contain excess chloride salts. This Cl has two fates: either excess salt diffuses through the cytoplasm to re-establish a new equilibrium with fixed anionic charges, or the excess salt is transported back across the membrane by cation-chloride cotransporters.[51-54] The transporters are required to re-establish the original steady state volume, but in the absence of transport, diffusion maintains local Cl concentrations remarkably well.[9, 52] In the absence of membrane Cl salt transport, this diffusion of excess Cl salts will be associated with either a cytoplasmic volume increase from associated water influx or an increase in the mean Cl concentration in the cytoplasm. At pathologically high rates of Cl influx, membrane chloride salt transport becomes rate-limiting,[51, 53, 55, 56] and chloride concentrations become sufficiently labile to depolarize E_{GABA}.[57-60] Thus Donnan exclusion *establishes* the local value of E_{GABA}, and active transport *maintains* that value (and neuronal volume) in the face of synaptic Cl flux.[10] The same principals should apply to the local extracellular chloride concentrations described here, with astrocytic chloride buffering[23] and diffusion between the extracellular fluid, the CSF, and vascular spaces[61] taking the place of neuronal membrane cation-chloride cotransport

Low extracellular Cl

The Cl^-_o measured by ABP FLIM is less than half of the canonical Cl^-_o. Such a low value of Cl^-_o should affect not only E_{GABA} but also the inhibitory $GABA_A$ conductance, because there are only half as many ions to carry the outward membrane currents (i.e. inward Cl- flux).[6] Shouldn't such a low value of Cl^-_o have been obvious from electrophysiological studies? E_{GABA} is determined by the ratio of Cl^-_i to Cl^-_o.[6, 62] If either concentration is known, the other can be determined from E_{GABA}. However if both Cl^-_i and Cl^-_o are determined by the concentrations of local immobile anions, neither can be set experimentally and thus E_{GABA} cannot be used to determine either Cl^-_i or Cl^-_o; only the ratio can be inferred from the Nernst equation. Similarly, although the conductance of inward Cl flux (outward membrane current) is determined in part by Cl^-_o, it is also determined by the $GABA_A$ permeability, i.e. the number of open membrane channels and their capacity for ion flux. Thus membrane currents are not sufficient to determine Cl^-_o.[6] Control of the ionic milieu is greater in single-channel recordings, but whether the complement of immobile anions is physiological under these conditions is difficult to determine, and even in these conditions there is substantial uncertainty regarding local ionic concentrations.[63]

Cl^-_o microdomains

The extracellular matrix of the brain is often depicted as perineural nets surrounding parvalbumin neurons that are detected by specific agglutinins and antibodies.[64] However, these assays detect very specific motifs of glycosaminoglycan sulfation; using more permissive ionic methods, a highly anionic extracellular matrix can be seen to surround virtually all neurons.[10, 20, 42] This extracellular matrix fills the extracellular space, which comprises about 20% of the brain's volume.[38, 65] The sGAG moieity of proteoglycans are the primary constituent of extracellular matrix.[17, 38] GAGs are polymers of widely varied length comprised of sugars and substituted sugars (N-acetylglucosamine, glucuronic acid, and galactose) that are synthesized without templates. Up to 3 sulfates are added to the sugar moieties before export to the extracellular space. This enables the creation of a stable but highly variable spatial distribution

of dense, fixed anionic charge in the extracellular matrix. Figure 3 demonstrates that this variance is substantial at the level of resolution of light microscopy. However, the distribution of fixed anions at the extracellular face of $GABA_A$ receptors, and the corresponding Cl^-_o, is currently unknown.

Physiological implications

Cl^-_o microdomains in the region of the extracellular openings of $GABA_A$ receptor-operated channels are a critical determinant of both E_{GABA} and the $GABA_A$ conductance. The wide range of Cl^-_o values established via Donnan exclusion by sulfated GAGs (Figures 2, 3, 4 and 5) makes possible a substantial variety of effects of $GABA_A$ receptor activation based on the direction of chloride flux. These effects range from hyperpolarizing inhibition through shunting inhibition through excitation by activation of low threshold calcium currents and removal of the magnesium block of the NMDA receptor. In addition, the effects of Cl^-_o on the quantity of charge that is carried by $GABA_A$ membrane currents (the conductance)[6] makes possible a broad range of strengths of $GABA_A$ synapses that is independent of the number or subunit composition of receptors or their posttranslational modifications.

The turnover of the macromolecules comprising the extracellular matrix is very slow,[66] on the order of months to years based on rodent experiments[67] as well as the rate of deterioration of patients with genetic defects of GAG catabolism.[68-70] This slow turnover provides a mechanism for long-lasting influences on synaptic GABA signaling. Some elements of GAG synthesis are activity dependent,[71] but currently nothing is known about the insertion of GAGs into the extracellular matrix, in situ modification, and the capacity for directed alterations of Cl^-_o microdomains in the regions of $GABA_A$ receptors and synapses. Thus the role of extracellular chloride microdomains in synaptic signal processing and memory remains to be discovered.

Pathological implications

Cytotoxic cerebral edema: If Cl^-_o is normally only half of the value of Cl in CSF and plasma, then the capacity for Cl^-_o to increase acutely may be an important and hitherto unappreciated element of the pathophysiology of cerebral edema.[72] Matrix metalloproteinases (MMPs) are released and activated after neuronal injury and death.[73] Release of sulfates in sGAGs from the extracellular matrix would reduce the Donnan exclusion of Cl by fixed sulfates. This would result in an acute increase of Cl^-_o as in Figure 4. The action of equilibrative cation-Cl cotransporters would then lead to a corresponding increase in chloride salts in the cytoplasm of neighboring healthy neurons, with attendant volume increases. This novel mechanism of cytotoxic edema could potentially be ameliorated by pharmacological MMP inhibition. Alternatively, inhibition of the influx of chloride salts that cross the BBB from the vascular space[74] would limit the influx of Cl into the extra and intracellular spaces.

Post Traumatic Epilepsy: Richard Miles and colleagues demonstrated that $GABA_A$ receptor activation could be excitatory in human brain tissue resected for control of medically intractable epilepsy.[75] However, the pathomechanism has never been elucidated.[8, 76, 77] Gliosis is the most common finding in medically intractable epilepsy.[78] In glial scars, reactive astrocytes synthesize new matrix elements.[79, 80] If the replacement matrix was more heavily sulfated than the original, as would be expected from the firm texture that is responsible for the name “scar,”[21] then in areas of gliosis Cl^-_o would be low. Low Cl^-_o could contribute to degradation of $GABA_A$ receptor mediated inhibition, frank excitation, and failure of anticonvulsants whose action are predicated on intact synaptic inhibition. Thus replacement of the extracellular matrix and distortion of

extracellular chloride microdomains could comprise an important mechanism of medically intractable epilepsy after brain injury.

Future studies

The findings that Cl^-_o is both lower than expected and spatially heterogenous opens the door for many investigations into the mechanisms by which Cl^-_o is set, such as the synthesis, export, and in situ modification of sulfated GAGs. The activity dependence of these mechanisms and the effect of Cl^-_o microdomains on synaptic signaling are additional areas of investigation. Pathologically, the impact of changes in Cl^-_o in both acute edema and long-term complications such as epilepsy may provide much-needed therapeutic insights into these frequently-intractable conditions.

Methods

General: Chemicals were purchased from Sigma-Aldrich (St Louis, MO) unless otherwise noted. Solutions are brought up in distilled water unless otherwise noted. Standard aCSF was brought up in 18MΩ water and consisted of (in mM): NaCl 126; KCl 3.5; $CaCl_2$ 2; $MgCl_2$ 1.3; NaH_2PO4 1.2; Glucose 11; $NaHCO_3$ 15. Low chloride aCSF variant was identical except that sodium gluconate was substituted for NaCl, resulting in 10mM Cl^-. Calibration solutions were made by mixing appropriate proportions of standard aCSF with low chloride aCSF such that a chloride and gluconate sum total of 136mM was maintained while Cl^- ranged from 10 to 136mM. Colorimetric assays were read using a Wallac Victor-2 1420 spectrophotometer with a halogen continuous wave light source and spectral line filters at listed wavelength +/- 5 to 10nm. Centrifugation steps were accomplished in a tabletop Eppendorf 5417R microcentrifuge. Reflux apparatus for synthesis consisted of a recirculating cooling bath (Fisher Scientific) filled with ethylene glycol cooling a 24/40 double-lumen coiled reflux tube (Ace Glassware, Vineland, NJ) with a 500mL round bottom flask (Corning) heated with a heating mantle regulated by a timed power controller (Glas-Col #O406 and #104A PL312, respectively).

Synthesis of ABP-dextran: The process of optimizing a bright, redshifted, pH-insensitive fluorophore that is responsive to chloride concentration over a dynamic range inclusive of expected extracellular chloride concentrations is beyond the scope of this paper and will be published separately (manuscript in preparation). Synthesis techniques closely followed those of the Verkman group when synthesizing related compounds[49, 81] and conjugating to dextran.[49] Briefly, N(4-***A***mino***B***utyl)***P***henantridinium (ABP) was synthesized by a reflux of equimolar amounts of phenanthridine and N(4-bromobutyl)phthalimide in acetonitrile followed by a second reflux in 6N HCl to hydrolyze phthalate. Product was twice recrystallized from 95% ethanol before conjugation to cyanogen bromide-activated 10,000g/moL (10KDa) dextran, producing 10KDa ABP-dextran with an approximate labeling ratio of 12.

Sulfation of agarose: We modified the method of Fuse and Suzuki[46] to add sulfate groups to the repeating disaccharide units of agarose; full details are supplied as a supplement. Briefly, agarose was dissolved in DMSO at 4% (w/v) at room temperature before being cooled to 4C and stirred with 0.4 volumes pre-chilled 4:1 acetic anhydride / glacial acetic acid for 15 minutes. Sulfuric acid (15.6M) is then added slowly at a 6:1 molar ratio to agarose repeating disaccharide units, taking care to keep temperature between 4-10°C. Mixture is then moved to ambient temperature and allowed to stir for 15 minutes before reaction is stopped by neutralization with 10M NaOH again taking care to avoid excessive heating. Sulfated agarose is then dialyzed at ambient temperature in 12-14KDa dialysis tubing (SpectraPor) against 15 volumes of 50mM Tris pH 7.4 once, then against distilled water changed twice daily until dialysate clarifies. Agarose is then precipitated in 95% ethanol, vacuum filtered, and oven-dried. Material is stored at ambient temperature in sealed glass vial until use.

Measurement of sulfate concentration in polysaccharide gels: $BaCl_2$-gelatin turbidimetric method[82] was used to quantify the sulfate content of gel materials. Sulfated agarose product or commercially available agarose or agar powder was dissolved in 0.5M HCl at a concentration of 5% (w/v) in 2mL screw-top microtubes with gasket (Fisher Scientific). Tubes are then placed in a heat block at 100-110°C for 3hours with periodic vortex mixing, hydrolyzing the sugar backbone and releasing sulfate. All samples had varying amounts of insoluble dark brown precipitated sugar, which was clarified at 20,000 x g for 10 minutes. Standards are diluted from 1M Na_2SO_4 stock in 0.5M HCl. $BaCl_2$-gelatin reagent is freshly prepared by dissolving 30mg

gelatin in 10mL distilled water at 80°C for 10minutes, then promptly adding 100mg $BaCl_2$ and vortex mixing. $BaCl_2$-gelatin is then allowed to cool passively before use. Samples are prepared by combining 1 part sample (diluted as desired), 1 part $BaCl_2$-gelatin, and 3 parts 0.5M HCl. Assay is performed in a glass-bottom 96-well plate reading absorbance at 405nm. Multiple sample dilutions were prepared and concentrations were calculated only from dilutions whose readings were well within the dynamic range of the standards.

Measurement of Cl^- in agar or agarose gels (chemical method): Chloride was measured colorimetrically using mercury(II) thiocyanate ($Hg(SCN)_2$) / iron(III) nitrate ($Fe(HNO_3)_3$) absorbance method of Florence and Farrar[83] to infer Cl^- from $Fe(SCN)_3$ production through the two-step reaction,

$$[\mathrm{Hg(SCN)_2} + 2\mathrm{Cl^-} \rightleftharpoons \mathrm{HgCl_2} + 2\mathrm{SCN^-}]\mathrm{x3}$$

$$[3\mathrm{SCN^-} + \mathrm{Fe(NO_3)_3} \rightleftharpoons \mathrm{Fe(SCN)_3} + 3(\mathrm{NO_3})^-]\mathrm{x2}$$

reading $Fe(SCN)_3$ absorbance at 490nm. Briefly, agar or agarose gels cast at 5% (w/v) in 3.5cm Petri dishes were drained by gravity and then Kimwipes were used to gently wick away remaining excess fluid at sides of dish. Similar amounts of each sample are transferred to 2mL screw-top microtubes with gasket (Fisher Scientific) and 1 gel volume, estimated by weight, of 7.8M nitric acid (HNO_3) is added (final [HNO_3] = 3.9M). Samples are then placed in a heat block at 100-110°C for 3hours with periodic vortex mixing, hydrolyzing the sugar backbone to break down the gel lattice. All samples had varying amounts of insoluble dark brown precipitated sugar, which was clarified at 20,000 x g for 10 minutes. A portion of supernatant or KCl standard, diluted with 0.3M HNO_3, was combined with one-tenth volumes of 0.4M $Fe(NO_3)_3$ (in 4M nitric acid) and saturated $Hg(SCN)_2$ (in ethanol), triturated, and allowed 20minutes for reaction to reach endpoint. Stock solutions are used within 1week. Multiple sample dilutions were prepared and concentrations were calculated only from dilutions whose readings were well within the dynamic range of the standards. Final concentrations are adjusted to account for dilution from original gel sample volume.

Fluorescence Lifetime Imaging (FLIM): Time-correlated single-photon counting (TCSPC) FLIM measurements were obtained using one of two custom MaiTai Ti:Sapph laser-scanning two-photon rigs with high-sensitivity PMT detectors. The first customized rig was used for early *in vitro* experiments and is detailed in the *in vitro* imaging section below; the second was custom made for *in vivo* experiments and is detailed in the *in vivo* imaging section below. In either case, ABP-dextran was excited at 760nm and emitted photons were subjected to a 445/58 bandpass filter prior to detection using high-sensitivity PMTs. Specific FLIM collection software differed between the two rigs and is detailed in the relevant sections below, but in either case a fluorescence lifetime is generated for each pixel by measuring the time it takes for an emitted photon to be detected, binning these photons according to arrival time, and to these data a first-order exponential equation is fit to derive the rate constant representing the fluorescence lifetime.[84] The presence of a quencher will shorten fluorescence lifetime to an extent which is linearly related to quencher concentration through the Stern-Volmer equation,

$$\frac{\tau_o}{\tau_i} = 1 + [Q]k_{SV}$$

where τ_o / τ_i represents the unquenched lifetime divided by the shortened lifetime at a given quencher concentration ([Q]).[84] The Stern-Volmer constant (k_{SV}) of the resultant line relates the

concentration of quencher to the shortening of fluorescence lifetime. Photons were collected over an acquisition period of 90 seconds (*in vivo* and agarose gels) to 150 seconds (*in vitro* slice cultures) and the lag between incident laser pulse and resulting photon detection recorded. The population of photons and associated lag times of each individual pixel is fit to an exponential to yield a lifetime value, and summed to yield an intensity value. ABP-dextran k_{SV} used in Cl^-_o calculations for a given experiment is derived from the specific batch of ABP-dextran calibrated on the specific microscope used and with settings used in the given experiment for which Cl^-_o is calculated. Image processing, calculations, and statistics were accomplished using built-in functions and custom routines developed in Matlab (v2018b and v2022a; Mathworks, Natick, MA).

Calibration of ABP-dextran: We initially calibrated ABP-dextran against chloride in simple phosphate buffer (20mM; pH 7.2) with varying amounts of NaCl (0-150mM), such that solutions were essentially modified PBS. We also verified whether other biologically relevant anions were capable of quenching ABP using similar buffers with 20mM phosphate and 0-150mM anion, or HEPES buffer (20mM; pH 7.2) when varying phosphate concentration. For subsequent experiments done in aCSF or *in vivo*, we calibrated ABP-dextran against aCSF with varying chloride concentrations (Figure 1B&C). This was accomplished by preparing standard aCSF (in mM: NaCl 126; KCl 3.5; $CaCl_2$ 2; $MgCl_2$ 1.3; NaH_2PO4 1.2; Glucose 11; $NaHCO_3$ 15) and a low-chloride aCSF in which NaCl was replaced with sodium gluconate, having demonstrated gluconate had no appreciable effect on ABP-dextran quenching (Figure 1C). We mixed appropriate amounts of this low chloride aCSF with standard aCSF to achieve varying chloride concentrations (10-136mM) in which the sum of sodium chloride and sodium gluconate was kept constant at 136mM. FLIM calibrations were obtained for each batch of ABP-dextran on the same microscope and with the same range of laser powers used in experiments, though k_{SV} did not appreciably change between ABP-dextran batches. Because calibrations done in aCSF have a minimum Cl^- of 10mM as described, the unquenched lifetime (τ_o) used for Stern-Volmer calculations is approximated as the y-intercept (Cl^- = 0mM) of a best-fit curve of the raw calibration data; empirically a biexponential fit was used (Figure 1B). All calculations are otherwise done as described under *Fluorescence Lifetime Imaging (FLIM)* section above. Notably, k_{SV} values did not differ appreciably between the aCSF and phosphate-buffered methods measured with the same rig.

Animals: All animal protocols were approved by the Massachusetts General Hospital Institutional Animal Care and Use Committee. Wild type mice (C57bl/6; Jackson Labs 000664) of either sex were used for this study. Mouse pups remained in the home cage with the dam under standard husbandry conditions until postnatal day 6 to 8 (P6–8) when organotypic slice cultures were prepared or until a cortical window was surgically placed at P26-30.

In vitro organotypic slice cultures and imaging: Organotypic hippocampal slice cultures were prepared either as glass-mounted[85] or membrane insert-mounted[86] cultures. Briefly, in either case hippocampi are obtained from P6-8 mice and cut to 400μm thick slices. These are then gently transferred to a 6-well dish containing either a membrane insert (Millipore) or a poly-L-lysine coated coverslip (Electron Microscopy Sciences), are fed twice weekly with 1mL neurobasal-A media supplemented with 500μM Glutamax, 2% B-27, and 0.03mg/mL gentamycin (all from Invitrogen), and are incubated at 35C in a 5% CO_2 incubator. Cultures are typically imaged between DIV 12-21 in aCSF warmed to 33°C and bubbled with 95%O_2 / 5% CO_2 perfused at a rate of approximately 100mL/hour unless otherwise noted. Slices were

pretreated with 500μg/mL ABP-dextran for 1-2 hours prior to perfusing with aCSF containing 136mM chloride and the same concentration of ABP-dextran. Slices were allowed to equilibrate in perfusate for 20-30 minutes before imaging, equaling at least 2 hours of total exposure to ABP-dextran prior to initiation of imaging. Two photon images were captured with a 20x water-immersion objective, NA 0.90, on a customized Olympus BX50WI rig equipped with an 80MHz Ti:Sapphire MaiTai laser (SpectraPhysics) driven with customized software for microscope operation and Becker & Hickl SPC800 FLIM hardware and software for data collection and initial processing in FLIM mode. Photons must pass through a 445/58 bandpass emission filter before PMT detection (Hamamatsu C6438-01). Lifetime and intensity values for each pixel are generated using SPCImage software (Becker & Hickl) before being exported for use in custom Matlab processing routines.

In vivo murine cortical window imaging: Using a modified method based on that of Che et al.,[87] we placed cortical windows in young adult mice (P26-30) for acute (non-survival) imaging in accordance with Massachusetts General Hospital Institutional Animal Care and Use Committee policies and procedures (protocol 2018N000221). Full methods are included as a supplement. Briefly, anaesthetized mice were immobilized with standard ear bars and nosepiece until custom headbar is placed (Figure 5A). A section of scalp is removed to expose a roughly 1cm section of skull. Acrylic dental cement powder (Lang Dental, Wheeling IL) mixed with cyanoacrylate adhesive is used to fix the headbar to the exposed skull at 4 o'clock to Bregma, creating a 5mm diameter working area. A 2.5mm round section of skull and underlying dura is removed and a 3mm No. 1 coverslip is placed over the exposed cortex. Coverslip has 10μL concentrated ABP-dextran / agarose mixture (1%w/v low gelation temperature agarose with 10mg/mL ABP-dextran in aCSF) pipetted from 42C heat block immediately before inversion and placement. One hour is allowed before image acquisition for ABP-dextran diffusion into cortex from overlying agarose (between cortex and coverslip; Figure 5B) during which time the warmed breadboard with immobilization apparatus and anesthetized mouse is transferred to the *in vivo* imaging microscope, a custom-made gantry-type two-photon microscope equipped with a MaiTai 80MHz Ti:Sapphire laser (Spectraphysics) and driven with customized ScanImage software (MBF Bioscience, Williston, VT). Photons are detected by a high-sensitivity PMT (Hamamatsu C5594-12) after passing through a 445/58 bandpass emission filter (Chroma) and digitized using custom ScanImage software. All other components are from Thor Labs. The initial analysis of raw FLIM data generating fluorescence lifetime data for each pixel is accomplished using ImageJ plug-in FLIMJ. Subsequent analysis including region of interest selection, conversion to chloride values (see below), composite image generation and statistics are accomplished using custom routines in Matlab.

Agarose or agar gel Cl^- determination using ABP-dextran FLIM: Cl^- within an agar or agarose gel was measured using the two-photon rig described above in the "in vivo" section, except with a 4x (NA 0.28) objective. Using an 8-well microchamber with silicone dividing gasket (Ibidi, Grafelfing, Germany), gels were cast in aCSF containing ABP-dextran and subsequently transferred to a single Petri dish where they were equilibrated with aCSF containing ABP-dextran for at least 1 hour prior to imaging. FLIM measurements were taken as described, generally one field per quadrant at a depth of between 50-100microns. Importantly, the gasket separating gels of differing compositions was removed such that all gels in an experiment were bathed in the same aCSF with the same Cl^- (Figure 2C). Where gels were kept for more than 1 day, they were prepared in aCSF without glucose and kept refrigerated between readings to prevent fouling.

Chondroitinase treatment of organotypic hippocampal slice cultures: Chondroitinase ABC (ChABC; AMSBIO, #E1028-02) was brought up in aCSF containing 0.1% bovine serum albumin (BSA) to a concentration of 1U/mL. Slices grown on membrane inserts were treated for 1hour either with aCSF containing ChABC or sham aCSF containing only the 0.1% BSA vehicle. Both experiment and control had 0.5mg/mL ABP-dextran (50μM), and FLIM imaging was done using the two-photon rig described in the *in vivo* section above. At the conclusion of imaging, the aCSF was collected for detection of liberated chondroitin sulfate.

Measurement of sulfated glycosamioglycans (sGAGs) liberated in aCSF: Blyscan 1,9-dimethylmethylene blue-based kit (Biocolor, #B1000) was utilized for measurement of sGAGs including chondroitin sulfate proteoglycans (CSPGs). After treatment with aCSF containing ChABC or BSA vehicle as detailed above, aCSF was collected and measured as directed against standards of bovine trachea chondroitin (Blyscan kit standard) with appropriate amounts of 10x stocks of aCSF and 0.1% BSA to obtain concentrations identical to samples. 1,9-Dimethylmethylene blue reagent absorbance is read at 650nm.

Image processing in Matlab: ABP fluorescence lifetime is converted to Cl^-_o as described above. Regions of interest (ROIs) are defined using intensity images for organotypic hippocampal slice cultures as a differentiation between tissue and surrounding bath or between anatomically defined regions such as the stratum pyramidale, stratum radiatum and stratum oriens. ROIs are defined *in vivo* as cortical regions between anatomical landmarks, such as vessels, which are identified through their exclusion of ABP-dextran. ROIs are then converted to masks and applied to fluorescence lifetime data, which are then converted to Cl^-_o. Variance of cortical Cl^-_o is measured against ABP-dextran in aCSF calibration solutions. Each concentration of Cl^- in the calibration curve has a normally distributed set of ABP-dextran lifetime values with a near-constant relative standard deviation (RSD = standard deviation divided by mean). Fluorescence lifetime has a physical upper and lower bound over which its values are meaningful (lifetime in the absence of quencher vs fully quenched fluorophore). Specifically for ABP-dextran we have found lifetime values to be linearly related to Cl^- from 0mM - 150mM through the Stern-Volmer relationship. We used these bounds for image processing as follows. Pixels were excluded (set to black) if ABP lifetimes were in excess of the mean at 0mM chloride, or if lifetimes were shorter than twice the standard deviation less than the mean at 150mM (calculated from best-fit curve to raw calibration data and average RSD). Excluding all values outside this calibrated range represents an average exclusion of 0.5-1.5% of pixels obtained using Becker&Hickl FLIM and 0.1-0.5% of pixels using the custom-built two-photon microscope described above. We then compared RSD values of ROIs to those of ABP-dextran in bulk solution to evaluate the extent of variation within differing regions. To assess the spatial distribution of local Cl^-_o, we modified methods recently developed to categorize intracellular chloride microdomains (Rahmati et al. 2021). Briefly, we binned Cl^-_o in a given field using uniform binwidths of <= 1mM over the range of mean +/- 2 standard deviations. Neighboring pixels that were in the same bin and whose raw values were within one bin width were considered to be a domain of chloride at the mid-bin Cl^-_o. These domains were then further characterized as described using custom Matlab routines.

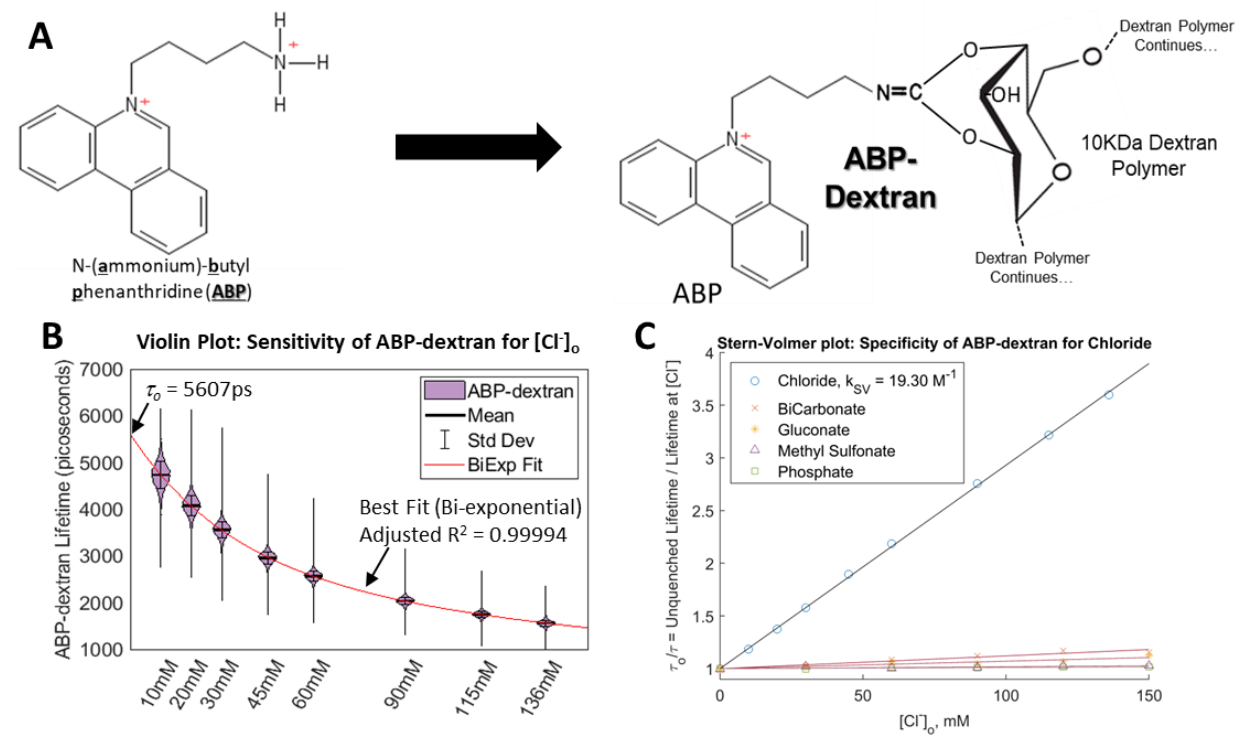

<u>Figure 1</u> Characterization and Calibration of Chloride-Sensitive Fluorophore ABP. ***A)*** N-(**<u>a</u>**mmonium)-**<u>b</u>**utyl **<u>p</u>**henanthridine (ABP) is synthesized in-house and conjugated to activated dextran, a glucose polymer, at a ratio of 10-14 fluorescent molecules per 10KDa Dextran. ***B)*** Representative calibration of ABP-dextran fluorescence lifetime versus Cl^- demonstrating ABP-dextran sensitivity to chloride-induced quenching. Calibration of ABP-dextran fluorescence lifetime vs Cl^-_o is displayed as a violin plot with mean +/- standard deviation overlaid. ABP-dextran lifetime at 0mM chloride (τ_o) is extrapolated using a best-fit approach (see Methods). ***C)*** Stern-Volmer plot demonstrates a linear relationship between ABP-dextran fluorescence lifetime and concentration of chloride and was used to convert lifetimes to chloride concentrations. The ratio of unquenched ABP-dextran fluorescence lifetime (τ_o) to ABP-dextran lifetime at a given concentration of quencher (τ) is plotted versus concentration of quencher (τ_o/τ vs $[Q^-]$). The slope of the linear regression is the Stern-Volmer constant (k_{SV}) which allows conversion of ABP-dextran lifetime to concentration of quencher, specifically Cl^- (blue circles / black line; k_{SV}=19.3M^{-1}). Four biologically relevant anions were found to have no experimentally relevant effect on ABP-dextran fluorescence lifetime: bicarbonate (k_{SV}=1.21M^{-1}), gluconate (k_{SV}=0.70M^{-1}), methyl sulfonate (k_{SV}=0.18M^{-1}), and phosphate (k_{SV}=0.11M^{-1}). Gluconate was subsequently used as a chloride substitute in non-standard aCSF formulations used for calibrations.

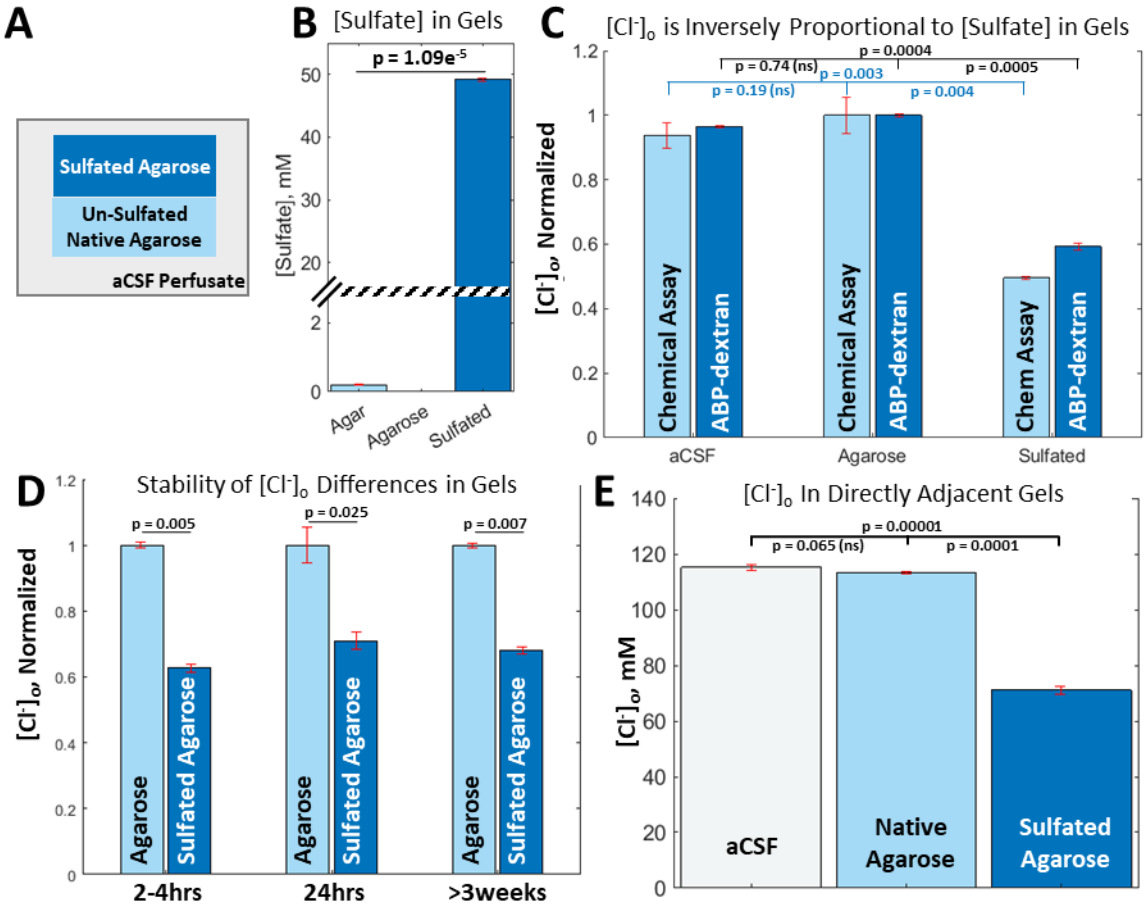

<u>Figure 2</u> Effects of immobile sulfate on Cl^- in a volume of agarose gel. ***A)*** Experimental schematic demonstrating how polysaccharide gels, cast in aCSF separately, were equilibrated in aCSF after transfer to a common vessel. Gels were either equilibrated with aCSF containing ABP-dextran, processed for chemical analysis, or subjected to multiple investigations in tandem (see Methods). ***B)*** We covalently bound sulfate groups to algal biopolymer agarose and cast this as a gel in aCSF to model perineuronal interstitial matrix that is rich in chondroitin sulfate-decorated glycosaminoglycans. We compared sulfated agarose gel to native agar and agarose gels, achieving a 250-fold increase in sulfate content compared to commercially available agar (bar 3 vs bar 1, respectively; note discontinuous y-axis). Commercially available agarose, which is intended as a sulfate-free product, had no measurable sulfate content (bar 2) and subsequently was used as a control gel. ***C)*** Chloride concentration was reduced in sulfated agarose gels. Cl^- was measured using both a standard colorimetric assay (light blue bars; statistics in blue) and ABP-dextran FLIM (dark blue bars; statistics in black) in aCSF control (leftmost pair), within non-sulfated agarose gel (center pair) and within sulfated agarose gel (rightmost pair) containing ≈50mM covalently bound sulfate. Measured chemically or using ABP-dextran FLIM, Cl^- in sulfated agarose gels differed significantly from aCSF and non-sulfated agarose gels, while Cl^- measured in non-sulfated agarose gels was not significantly different from aCSF. ***D)*** Significant chloride concentration differences between agarose gels with ≈50mM covalently bound sulfate (dark blue) and non-sulfated agarose gels (light blue) do not equilibrate with time but instead are stable for as long as experimentally observed (> 3 weeks). ***E)*** Demonstration of stable juxtaposition of significantly different chloride concentrations

at equilibrium. Separately cast sulfated and non-sulfated gel pieces are placed in a single vessel as described in ***A*** and equilibrated in common aCSF with ABP-dextran. Sulfated agarose gels (dark blue) again contain significantly lower Cl^- than do non-sulfated agarose gels (light blue) or perfusate aCSF (gray). Cl^- within non-sulfated agarose gels is not significantly different than perfusate aCSF. *Statistical significance was determined using Student's unpaired (D) or paired (B,C&E) t-test with indicated p-values; "ns" indicates "not significant".*

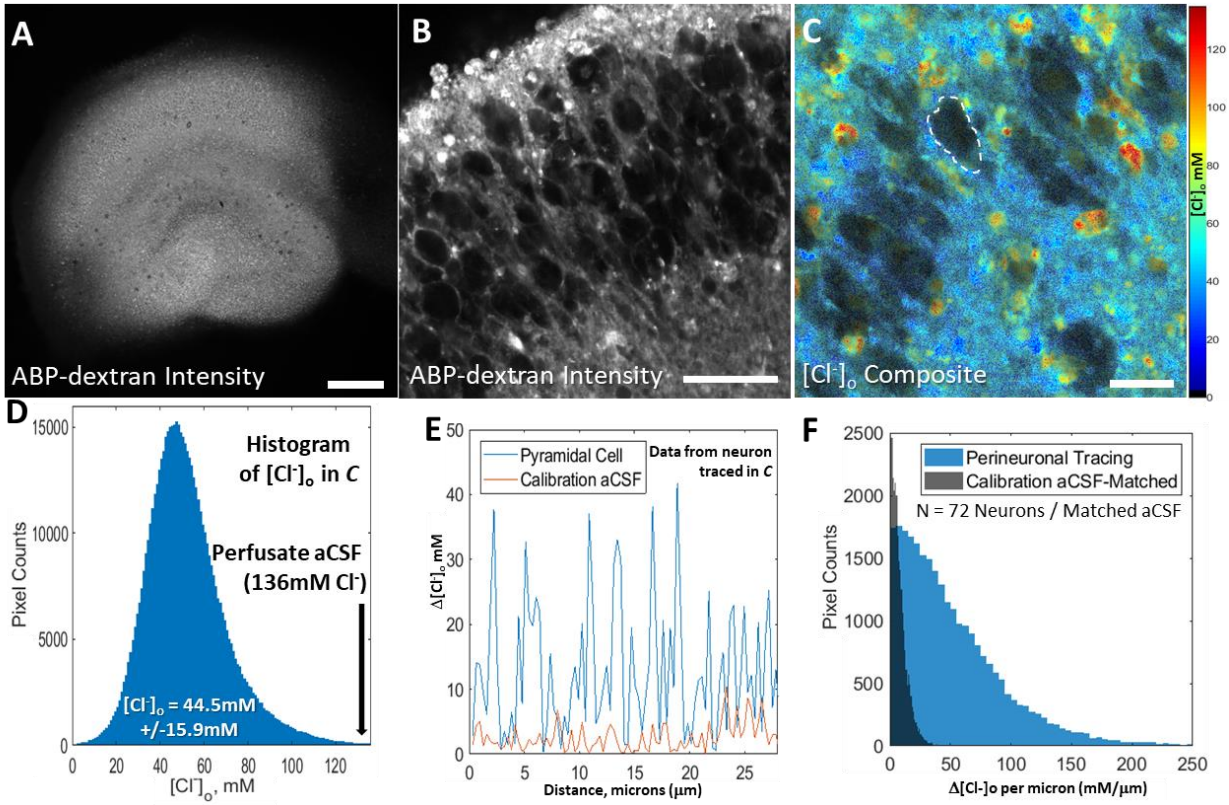

<u>Figure 3</u> Cl^- in the extracellular space is not uniform and is considerably lower than aCSF perfusate. ***A)*** Low-magnification intensity image of representative mouse hippocampal slice culture (HSC) demonstrating exclusion of ABP-dextran from cell bodies, particularly in CA1, and brighter signal of ABP-dextran within the HSC corresponding to longer lifetimes (lower Cl^-_o) versus surrounding aCSF perfusate where ABP-dextran is near-fully quenched (scale bar 500μm). ***B)*** High-magnification HSC intensity image of ABP-dextran excluded from cell bodies in the pyramidal cell layer (CA1; scale bar 20μm). ***C)*** Chloride-composite image again demonstrating the exclusion of ABP-dextran from intracellular spaces as well as the non-uniformity of Cl^-_o in the pyramidal cell layer of a representative HSC. Representative pyramidal cell visible just above and left of image center, and identified by ABP-dextran exclusion and morphology of resulting silhouette, is one of 6-10 neurons per field deemed to have a regular and nearly-continuous border analyzed as described in ***E&F*** (scale bar 20μm). ***D)*** Histogram of full field Cl^-_o in HSC pictured in ***C***, demonstrating non-uniformity visually apparent in ***C***. Notably, Cl^-_o = 44.5+/-15.9mM despite perfusate $[Cl^-]$ = 136mM (across all depths of this slice Cl^-_o = 49.7+/-18.5mM; mean +/- standard deviation). ***E)*** Change in chloride ($\Delta[Cl^-]_o$) plotted against distance in the perineuronal space (blue line) or the same trace overlaid onto a calibration aCSF FLIM image (red line) corresponding to the perineuronal trace in ***D***. $\Delta[Cl^-]_o$ of calibration aCSF (red) encapsulates machine and experimental noise, and $\Delta[Cl^-]_o$ in the perineuronal space (blue) exceeds that of control calibration aCSF in this representative neuron's perineuronal space. ***F)*** Perineuronal $\Delta[Cl^-]_o$ per micron calculated from many neurons' circumferential traces

demonstrates that the variability of Cl^-_o just outside neurons in a living system exceeds the variability of control aCSF (72 neurons or matched calibration aCSF controls from depths of 20-100microns in this representative HSC). *Scale bars: A 500μm; B 50mm D 20μm.*

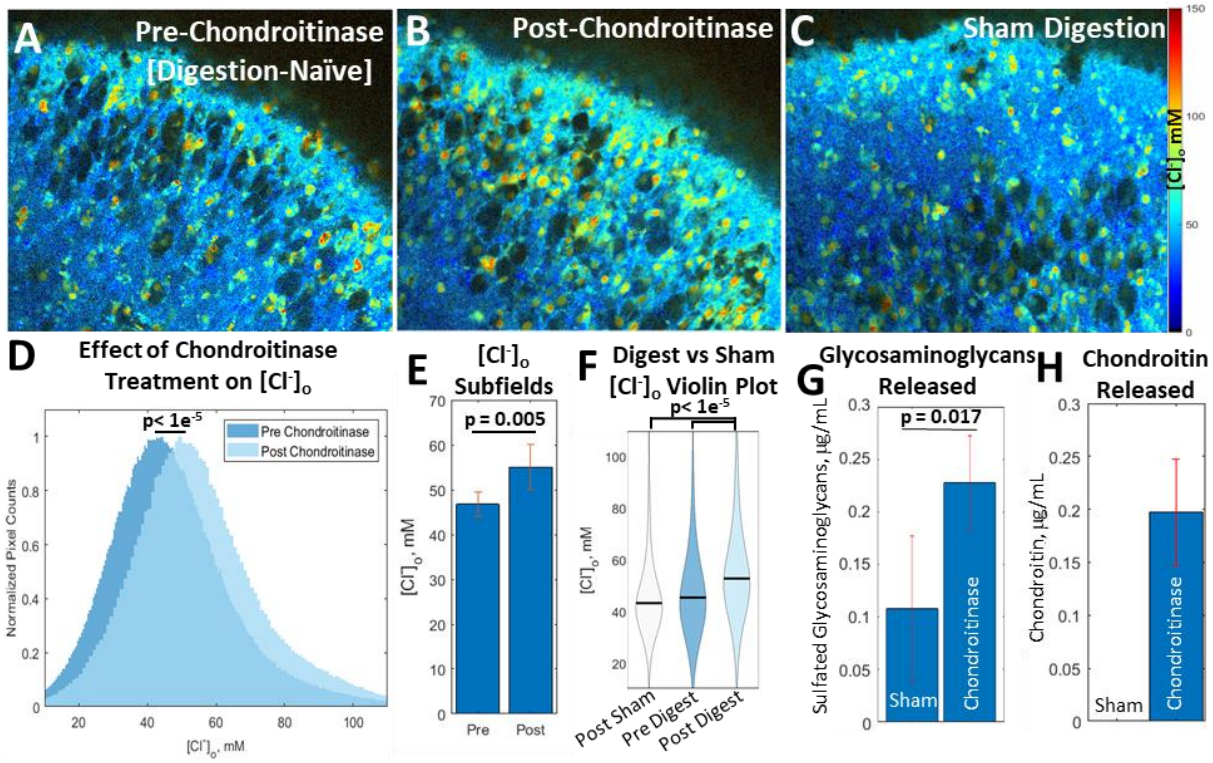

<u>Figure 4</u> Chondroitinase treatment removes fixed perineuronal anions and attenuates Cl^-_o displacement. ***A-C)*** Cl^-_o composite images of representative mouse hippocampus slice cultures imaged in culture media ($Cl^- \approx 64$mM) with 1mg/mL ABP-dextran (100µM ABP-Dextran) before (***A***) and after (***B***) treatment with bacterial MMP analog chondroitinase, or after sham digestion (***C***); shared colorbar for ***A-C*** at right. ***D)*** Histograms of $[Cl^-]_o$ corresponding to ***A&B***. Pre-chondroitinase digestion (dark blue) and post-chondroitinase digestion (light blue) $[Cl^-]_o$ populations of pixels are significantly different. ***E)*** When images from ***A&B*** are broken into 8 regularly shaped regions of interest and analyzed as paired sets of groups, pre-chondroitinase and post-chondroitinase are again significantly different (46.7+/-2.7mM vs 55.0+/- 5.0mM, respectively). ***F)*** Violin plot of data from A&B (dark and light blue, respectively) vs grouped sham-digested slice data (gray) demonstrating that Cl^-_o increases significantly after chondroitin sulfate is removed by digestion. ***G)*** Measurement of glycosaminoglycans, including chondroitin sulfate, released into the perfusate after slice cultures are treated with chondroitinase (vs sham digestion) using a commercial colorimetric assay. A significantly higher concentration of polyanions are found in the extracellular fluid after chondroitinase digestion, consistent with the release of chondroitin sulfate from extracellular matrix within slice cultures and a resultant increase in Cl^-_o. ***H)*** HPLC analysis confirms the presence of chondroitin sulfate in digestion buffer after chondroitinase treatment (mean = 0.20µg/mL); there was no detectable chondroitin sulfate in sham digests. *All slice cultures were DIV14-21 at time of experiment; cultures were grown directly on glass with the exception of **F** where cultures were grown on membrane inserts (see Methods); **D&F** significance at $p < 1e^{-5}$ level by Kolmogorov-Smirnov paired-sample test applied to distributions;* **E** *significance at p = 0.0052 by paired t-test of regular ROIs; **G** significance at p = 0.05 level by paired t-test (p = 0.017); **H** significance was not formally*

*determined as no signal could be detected in sham-digested controls. Note that data contained in **D-F** labeled 'pre' and 'post' are derived from **A** and **B**, respectively.*

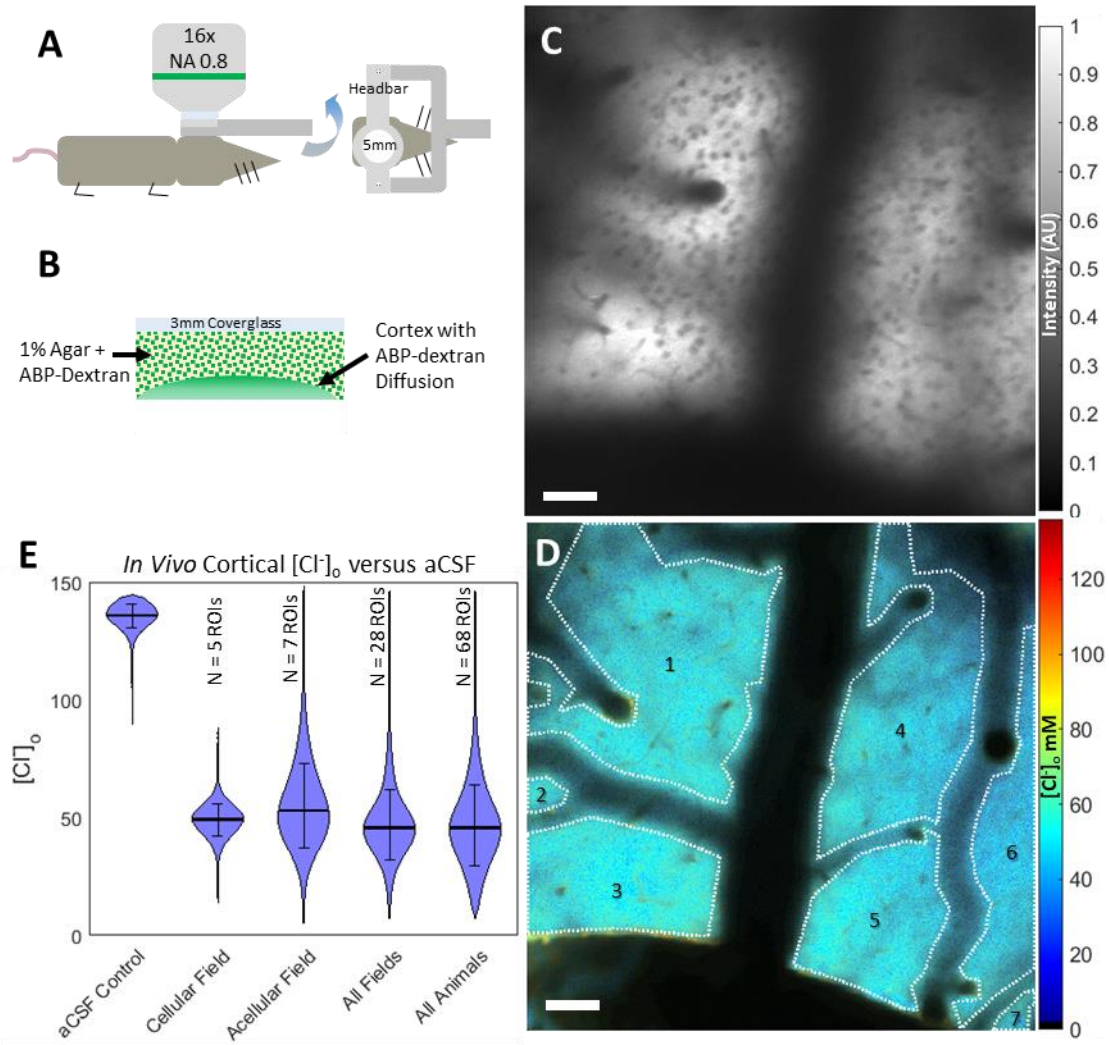

<u>Figure 5</u> *In vivo* Cl^-_o in mouse neocortex is consistent with *ex vivo* findings. ***A-B)*** Schematic of in vivo imaging set-up, using a surgically implanted headbar to immobilize P26-P30 mouse pup for imaging through 3mm coverglass window overlaying 1% agar brought up in aCSF containing ABP-Dextran and 136mM chloride laid directly on exposed cortex. ***C)*** Intensity image of mouse L2/3 cortex, demonstrating ABP-dextran exclusion from cells and vessels; large vessels appear blurred because their widest diameter exists superficial to this field (scale bar 50μm). ***D)*** Chloride composite image corresponding to L1 cortex 138μm superficial to field ***C***. ROI selection excludes vessels but is otherwise permissive as demonstrated here. More examples can be found in **Figure S5** (scale bar 50μm). ***E)*** Cl^-_o in mouse neocortex is significantly lower than the CSF Cl^-. Violin plot with population mean and standard deviations overlaid. Compared to agarose brought up in 136mM aCSF overlying the cortex (135.4+/-5.0mM, leftmost plot), *in vivo* mouse cortex had significantly lower Cl^-_o whether measured in cellular fields such as in ***C*** or in acellular fields such as in **D** (48.9+/-6.7mM and 55.0+/-17.9mM, respectively, plots 2 and 3). This was also true when taking all fields from this representative animal together and when taking all fields from all animals used in this study (47.2+/-14.9mM and 48.1+/-17.0mM, respectively, plots 4 and 5).

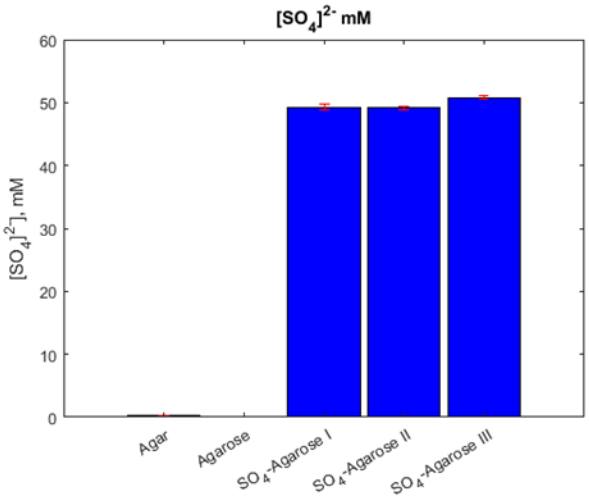

<u>Supplemental Figure S1:</u> Reliability of agarose sulfation. Commercially available, naturally sulfated agar has < 1mM sulfate while commercially available agarose has no measurable sulfate in our hands (bars 1 and 2, respectively). Each of three consecutive batches of sulfated agarose ("SO_4-Agarose" I, II, and III; bars 3-5) are consistently found to have ≈50mM sulfate by barium chloride precipitation (see Methods). The amount of sulfate in agar was experimentally negligible (250-fold difference vs sulfated).

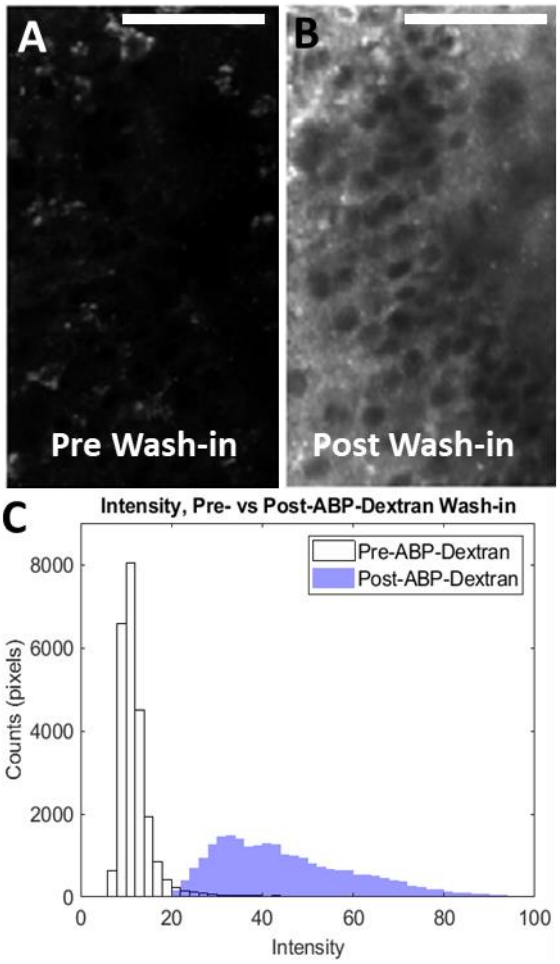

<u>Supplemental Figure S2</u> Specificity of ABP-dextran signal for extracellular space. ***A&B)*** Intensity images of hippocampal slice culture (HSC) CA1 pyramidal cell layer acquired with identical settings prior to (***A***) and 90 minutes after (***B***) ABP-dextran wash-in, demonstrating both the scarcity of background signal in wild-type tissue used in this study and the exclusion of ABP-dextran from the pyramidal cell layer; scale bar 500μm. ***C)*** Quantification of intensity images in **A&B**. Wider distribution of ABP-dextran intensity corresponds to varied areas of exclusion, such as intracellular space, to which ABP-dextran does not have access. Higher minimum intensity (background) is likely due to out of focus light just above or below the focal plane; higher resolution images do not demonstrate the same phenomenon (see **Figure 3B**). *Scale bar:* ***A&B*** *500μm.*

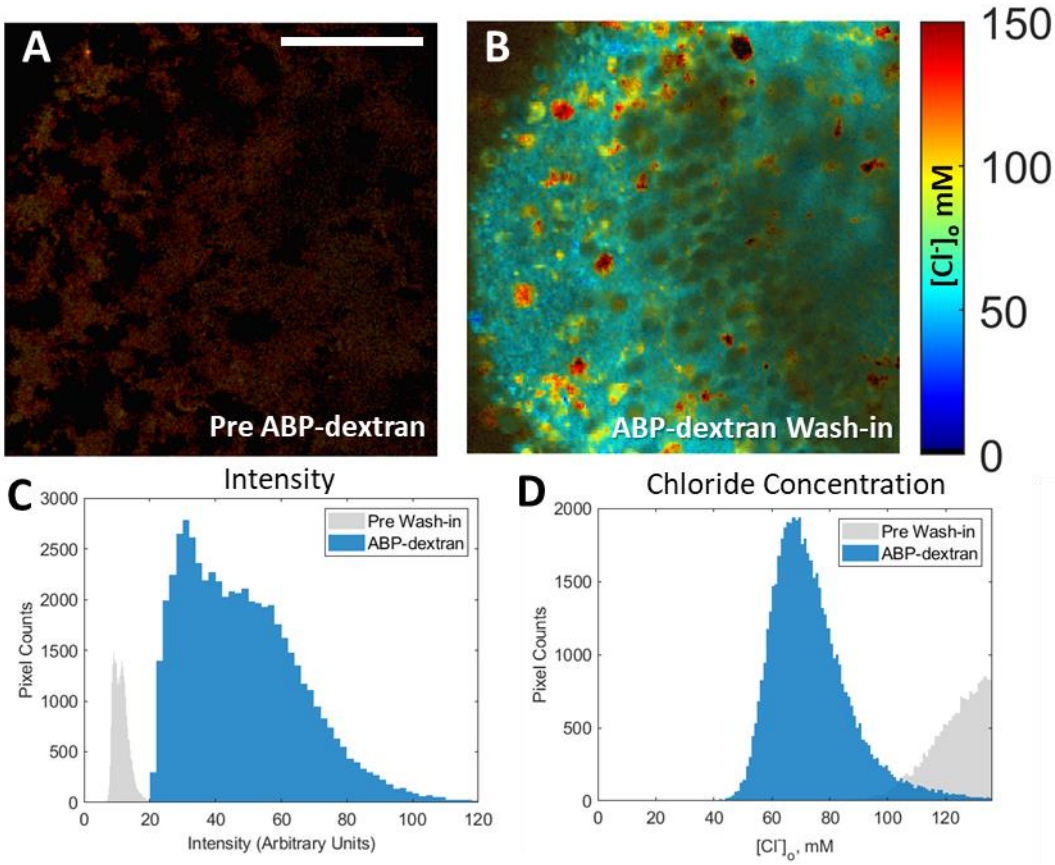

<u>Supplemental Figure S3</u> Specificity of ABP-dextran signal for Cl-o. ***A&B)*** Chloride composite images of hippocampal slice culture (HSC) acquired and rendered with identical settings prior to (***A***) and 90minutes after (***B***) ABP-dextran wash-in, demonstrating 1) the scarcity of background signal in wild-type tissue used in this study; 2) the exclusion of ABP-dextran from the pyramidal cell layer (***B*** vs ***A***); 3) and the fact that background signal, likely autofluorescent in origin, has a characteristically short lifetime and if impactful on our measurements would cause artificially high chloride readings (due to shortening of calculated lifetime). Shared colorbar to right of ***B***; scale bars 500μm. ***C)*** Intensity histograms of pre- and post-ABP-dextran wash-in (***A&B***) quantifying the relative paucity of fluorescence signal from the pre-wash-in image. ***D)*** Those pixels with sufficient intensity to calculate fluorescence lifetime are converted to Cl^-_o (***B***) and quantified by histogram, demonstrating little overlap between the two populations. *Scale bar:* ***A&B*** *500μm.*

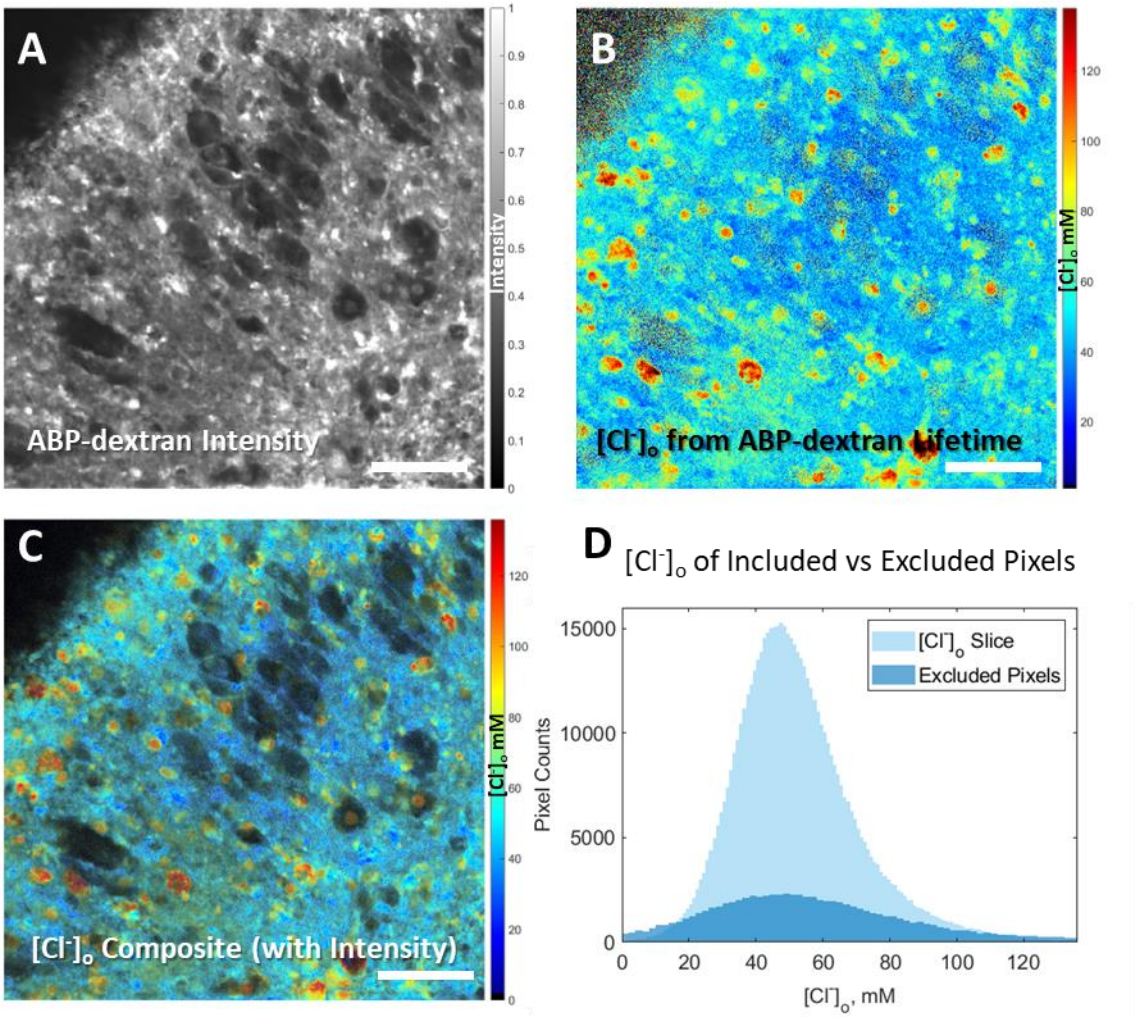

<u>Supplemental Figure S4:</u> Generation of composite chloride images and cell body masking for pixel quantification. ***A)*** ABP-dextran intensity data of an HSC, derived by taking the total number of photons detected in each pixel throughout the acquisition period, is used to inform on tissue structure. ***B)*** Cl^-_o calculated from ABP-dextran lifetime. The loss of discernible structure is due to the fact that the intensity of the ABP-dextran signal has no effect on the Cl^-_o calculated, only the lifetime as calculated from the population of photons gathered in each pixel (see Methods). ***C)*** In order to observe Cl^-_o with spatial context restored, we use intensity data to inform the alphadata property of the raw chloride data in ***B***, generating a composite image in which the color corresponds to Cl^-_o but the brightness of each pixel is attenuated based on the intensity of the signal (see Methods). Similar methods of composite display are utilized by the most popular proprietary software. ***D)*** Quantification of Cl^-_o in pixels retained and pixels excluded in this HSC. Excluded pixels, i.e. those pixels that had sufficient signal to calculate a fluorescence lifetime but were under a manually defined intensity threshold, can be seen to have a similar mode and span a similar range of chloride values. Notably, very low Cl^-_o (i.e., =< 15mM) pixels, corresponding to typical intracellular Cl^- values, are more likely excluded than not. *Scale bar:* ***A-C*** *50μm.*

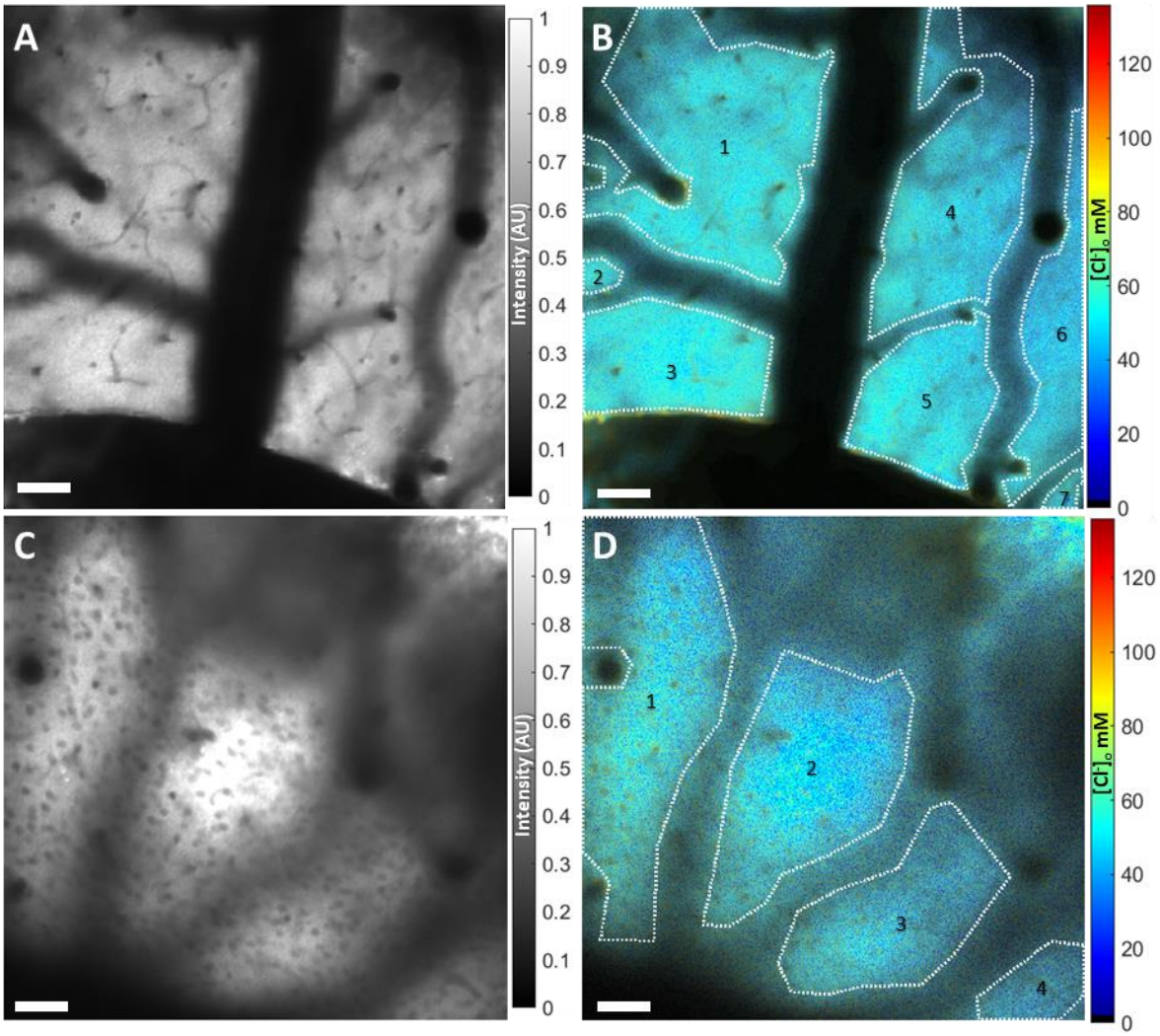

<u>Supplemental Figure S5:</u> ***In vivo*** **Cl^-_o examples of cellular and acellular fields**. ***A&B)*** Intensity (***A***) and Cl^- composite (***B***) images of mouse L1 neocortex. Exclusion of ABP-dextran from vessels is most evident in A, with some out of focus vessels causing discernible shadows. ***C&D***) Intensity (***C***) and Cl^- composite (***D***) pair from a deeper field (L2/3 neocortex) demonstrating ABP-dextran exclusion from cells. Small vessels evident in ***A*** are also seen in ***B***, and cell bodies seen in ***C*** are also evident in ***D***. ROIs are selected and overlaid in Cl^- composite images (***B&D***; white dashes); these are assigned intensity thresholds individually to account for varying brightness within the same field. Importantly, pixels excluded by thresholding did not have characteristic Cl^-_o but generally spanned the full range of the Cl^-_o found elsewhere in the field (see Figure S4D). *All scale bars: 50μm*.

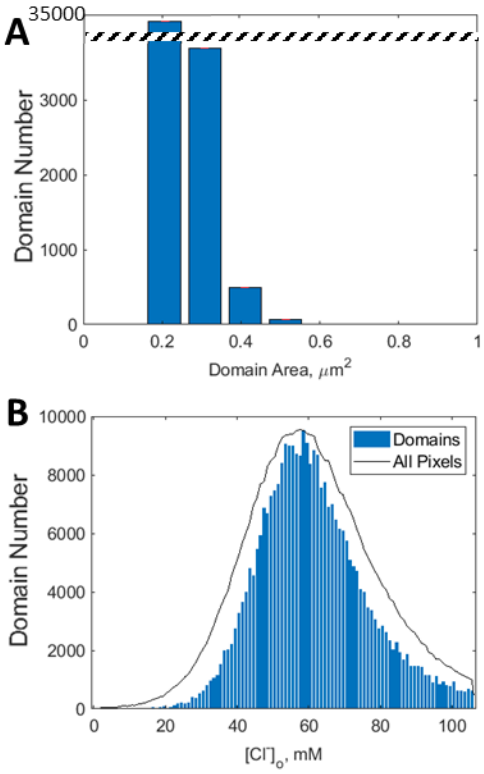

<u>Supplemental Figure S6</u>: Extracellular microdomains of Cl^-. In the same high-magnification, diffraction-limited resolution slice seen in **Figure 3**, we attempted to identify and characterize Cl^-_o microdomains in a manner similar to our recent work on intracellular chloride. ***A)*** Nearly 90% of multiple pixel areas with Cl^-_o within 1mM of each other were the smallest measurable area, indicating that the size of such domains may be smaller than our resolution. ***B)*** There was no particular Cl^-_o range that was more likely to be identified as part of a chloride microdomain, i.e. Cl^-_o values within domains mirrored that of all pixels taken together.

Supplemental Methods:

Sulfation of Agarose: The goal of maximizing sulfation must be balanced with the consequent erosion of gel properties such as gelation and water holding capacity. Agarose was added to a well-dried Erlenmeyer flask and dissolved in DMSO at a concentration of 4%(w/v) at room temperature before being cooled to 4°C with stirring. Addition of 4:1 mixture of acetic anhydride / glacial acetic acid, also pre-chilled to 4°C, was added to agarose/DMSO mixture (2 parts to 5 parts). Vigorous mixing by hand was necessary to thin the gelatinous mixture to a slurry and allow stirring at 4°C for 15 minutes; gentle heat transfer from experimenter's hands likely helped loosen the initial gel but care is taken to return the mixture to 4°C. Concentrated sulfuric acid is then added slowly at specified molar ratio to repeating disaccharide unit, D-galactose – 3,6-anhydro-L-galactopyranose, at 4°C with stirring. Diluted sulfuric acid should be avoided, as the presence of water under acidic conditions promotes hydrolysis of the polymer and diminishes gelation. Mixture is then allowed to stir at ambient temperature for an additional 15 minutes. The reaction is then stopped by neutralization with 10M NaOH, again with stirring at 4°C. This is also an exothermic process; mixture is chilled in an ice bath prior to and periodically during neutralization. Ideal temperature is 10-15°C and is not allowed to exceed room temperature. 10M NaOH neutralization unavoidably adds water to the acidic mixture, which promotes hydrolysis of the polymer and must be done with as much haste as tolerable while keeping the temperature of the solution in the specified range. Once 90% of the calculated base necessary to neutralize the solution has been added, pH is monitored with a 3-point calibrated pH meter (insert specifics) until a weakly basic pH is achieved (7.20). Sulfated agarose is then dialyzed in 12-14KDa dialysis tubing (SpectraPor, S432703) against 15 volumes of 50mM Tris pH 7.4 for 2-3 hours, then distilled water changed twice daily until dialysate clarifies. Agarose is then precipitated by adding 200-proof ethanol to achieve 95% ethanol/water and cooling to 4C at least 4hours. Vacuum filtered material was subsequently dried in 50C oven as an alternative to lyophilization. Material is stored at ambient temperature in sealed glass vial until use.

Fluorescence Lifetime Imaging (FLIM): Time-correlated single-photon counting (TCSPC) FLIM measurements were obtained using one of two custom MaiTai Ti:Sapph laser-scanning two-photon rigs with high-sensitivity PMT detectors. The first customized rig was used for early in vitro experiments and is detailed in the in vitro imaging section below; the second was custom made for in vivo experiments and is detailed in the in vivo imaging section below. In either case, ABP-dextran was excited at 760nm and emitted photons were subjected to a 445/58 bandpass filter prior to detection using high-sensitivity PMTs. Specific FLIM collection software differed between the two set-ups and is detailed in the relevant sections below, but in either case each pixel had an associated histogram expressing photon number vs photon travel time (the delay between excitation and detection) which was fitted to a single exponential curve to derive a time constant *k*,

$$(1)\ A_t = A_o e^{-kt}$$

denoting the fluorescence lifetime of the fluorophore derived from each pixel. As implied by Equation 1, fluorescence lifetime is an intrinsic property of the fluorophore and wholly independent of fluorophore concentration. However, fluorescence lifetime may be shortened (i.e., quenched) by one or more moieties in a manner dependent upon the concentration of the quencher – *not the concentration of the fluorophore itself*. In the case of the fluorophore used in the present study (ABP), chloride is the lone biologically relevant quencher. The degree of

lifetime shortening relative to the initial unquenched lifetime is linearly related to the concentration of the quencher through the Stern-Volmer relationship,

$$(2)\ \frac{\tau_o}{\tau_i} = 1 + [Q]k_{SV}$$

where τ_o / τ_i represents the unquenched lifetime divided by the shortened lifetime at a given quencher concentration ([Q]), necessarily yielding a y-intercept of 1 (Gehlen, 2020). The slope of the resultant plot, referred to as the Stern-Volmer constant (k_{SV}), facilitates conversion of measured fluorescence lifetime to concentration of quencher. Notably, there is no term to describe fluorophore concentration in Equation 2 as the fluorophore concentration has no impact on measured lifetime. Only the concentration of the quencher, chloride, affects the fluorescence lifetime. Images are acquired over 1.5 minutes (*in vivo* and agarose gels) to 2.5 minutes (*in vitro* slice cultures), with each pixel having a histogram of photons populating time bins from which a single exponential time constant (fluorescence lifetime) and intensity value (summed photons from all bins) are derived. Utilizing the k_{SV} derived from the specific batch of ABP-dextran used in a given experiment and calibrated on the same microscope used under experimental conditions and settings, Cl^-_o is calculated in living tissue or in agarose gels from lifetime values. These calculations, as well as intensity-based region of interest selection and subsequent processing, is accomplished using built-in functions and custom routines developed in Matlab (v2018b and v2022a; Mathworks, Natick, MA) using signal processing and statistics toolboxes.

Bibliography

1. Hu, H., Gan, J. & Jonas, P. Interneurons. Fast-spiking, parvalbumin^{+} GABAergic interneurons: from cellular design to microcircuit function. *Science* **345**, 1255263 (2014).
2. Tremblay, R., Lee, S. & Rudy, B. GABAergic Interneurons in the Neocortex: From Cellular Properties to Circuits. *Neuron* **91**, 260-292 (2016).
3. Thompson, S.M., Deisz, R.A. & Prince, D.A. Relative contributions of passive equilibrium and active transport to the distribution of chloride in mammalian cortical neurons. *J Neurophysiol* **60**, 105-124 (1988).
4. Staley, K.J. & Mody, I. Shunting of excitatory input to dentate gyrus granule cells by a depolarizing GABAA receptor-mediated postsynaptic conductance. *J Neurophysiol* **68**, 197-212 (1992).
5. Tyzio, R.*, et al.* Postnatal changes in somatic γ-aminobutyric acid signalling in the rat hippocampus. *European Journal of Neuroscience* **27**, 2515-2528 (2008).
6. Coombs, J.S., Eccles, J.C. & Fatt, P. The specific ionic conductances and the ionic movements across the motoneuronal membrane that produce the inhibitory post-synaptic potential. *J Physiol* **130**, 326-374 (1955).
7. Ebihara, S., Shirato, K., Harata, N. & Akaike, N. Gramicidin-perforated patch recording: GABA response in mammalian neurones with intact intracellular chloride. *J Physiol* **484 (Pt 1)**, 77-86 (1995).
8. Huberfeld, G.*, et al.* Perturbed chloride homeostasis and GABAergic signaling in human temporal lobe epilepsy. *J Neurosci* **27**, 9866-9873 (2007).
9. Rahmati, N.*, et al.* Unique Actions of GABA Arising from Cytoplasmic Chloride Microdomains. *J Neurosci* **41**, 4957-4975 (2021).
10. Glykys, J.*, et al.* Local impermeant anions establish the neuronal chloride concentration. *Science* **343**, 670-675 (2014).
11. Marinsky, J.A. An interpretation of the sensitivity of weakly acidic (basic) polyelectrolyte (cross-linked and linear) equilibria to excess neutral salt. *Journal of physical chemistry (1952)* **89**, 5294--5302 (1985).
12. Helfferich, F. *Ion Exchange* (Dover, New York, NY, 1995).
13. Fatin-Rouge, N., Milon, A., Buffle, J., Goulet, R.R. & Tessier, A. Diffusion and partitioning of solutes in agarose hydrogels: the relative influence of electrostatic and specific interactions. *The Journal of Physical Chemistry B* **107**, 12126-12137 (2003).
14. Epsztein, R., Shaulsky, E., Dizge, N., Warsinger, D.M. & Elimelech, M. Role of Ionic Charge Density in Donnan Exclusion of Monovalent Anions by Nanofiltration. *Environ Sci Technol* **52**, 4108-4116 (2018).
15. Gao, K.W., Yu, X., Darling, R.M., Newman, J. & Balsara, N.P. Increased Donnan exclusion in charged polymer networks at high salt concentrations. *Soft Matter* **18**, 282-292 (2022).
16. Sola, M., Kneussel, M., Heck, I.S., Betz, H. & Weissenhorn, W. X-ray crystal structure of the trimeric N-terminal domain of gephyrin. *J Biol Chem* **276**, 25294-25301 (2001).
17. Karamanos, N.K.*, et al.* A guide to the composition and functions of the extracellular matrix. *Febs j* **288**, 6850-6912 (2021).
18. Urban, J.P., Maroudas, A., Bayliss, M.T. & Dillon, J. Swelling pressures of proteoglycans at the concentrations found in cartilaginous tissues. *Biorheology* **16**, 447-464 (1979).
19. Chahine, N.O., Chen, F.H., Hung, C.T. & Ateshian, G.A. Direct measurement of osmotic pressure of glycosaminoglycan solutions by membrane osmometry at room temperature. *Biophys J* **89**, 1543-1550 (2005).
20. Morawski, M.*, et al.* Ion exchanger in the brain: quantitative analysis of perineuronally fixed anionic binding sites suggests diffusion barriers with ion sorting properties. *Scientific reports* **5**, 16471 (2015).

21. Lesperance, L.M., Gray, M.L. & Burstein, D. Determination of fixed charge density in cartilage using nuclear magnetic resonance. *J Orthop Res* **10**, 1-13 (1992).
22. Titze, J.*, et al.* Glycosaminoglycan polymerization may enable osmotically inactive Na+ storage in the skin. *Am J Physiol Heart Circ Physiol* **287**, H203-208 (2004).
23. Egawa, K., Yamada, J., Furukawa, T., Yanagawa, Y. & Fukuda, A. Cl^- homeodynamics in gap junction-coupled astrocytic networks on activation of GABAergic synapses. *J Physiol* **591**, 3901-3917 (2013).
24. Kuang, D. & Hampson, D.R. Ion dependence of ligand binding to metabotropic glutamate receptors. *Biochem Biophys Res Commun* **345**, 1-6 (2006).
25. Plested, A.J. & Mayer, M.L. Structure and mechanism of kainate receptor modulation by anions. *Neuron* **53**, 829-841 (2007).
26. Kusama, N., Harding, A.M. & Benson, C.J. Extracellular chloride modulates the desensitization kinetics of acid-sensing ion channel 1a (ASIC1a). *J Biol Chem* **285**, 17425-17431 (2010).
27. DiRaddo, J.O.*, et al.* Chloride is an Agonist of Group II and III Metabotropic Glutamate Receptors. *Mol Pharmacol* **88**, 450-459 (2015).
28. Tora, A.S.*, et al.* Chloride ions stabilize the glutamate-induced active state of the metabotropic glutamate receptor 3. *Neuropharmacology* **140**, 275-286 (2018).
29. Zhang, Y.W.*, et al.* Chloride-dependent conformational changes in the GlyT1 glycine transporter. *Proc Natl Acad Sci U S A* **118** (2021).
30. Jiang, C., Agulian, S. & Haddad, G.G. Cl- and Na+ homeostasis during anoxia in rat hypoglossal neurons: intracellular and extracellular in vitro studies. *J Physiol* **448**, 697-708 (1992).
31. Kroeger, D., Tamburri, A., Amzica, F. & Sík, A. Activity-dependent layer-specific changes in the extracellular chloride concentration and chloride driving force in the rat hippocampus. *J Neurophysiol* **103**, 1905-1914 (2010).
32. Grimley, J.S.*, et al.* Visualization of synaptic inhibition with an optogenetic sensor developed by cell-free protein engineering automation. *J Neurosci* **33**, 16297-16309 (2013).
33. Sato, S.S.*, et al.* Simultaneous two-photon imaging of intracellular chloride concentration and pH in mouse pyramidal neurons in vivo. *Proceedings of the National Academy of Sciences* **114**, E8770-E8779 (2017).
34. Biwersi, J., Farah, N., Wang, Y.X., Ketcham, R. & Verkman, A.S. Synthesis of cell-impermeable Cl-sensitive fluorescent indicators with improved sensitivity and optical properties. *Am J Physiol* **262**, C242-250 (1992).
35. Biwersi, J., Tulk, B. & Verkman, A.S. Long-wavelength chloride-sensitive fluorescent indicators. *Anal Biochem* **219**, 139-143 (1994).
36. Kaneko, H., Putzier, I., Frings, S., Kaupp, U.B. & Gensch, T. Chloride accumulation in mammalian olfactory sensory neurons. *J Neurosci* **24**, 7931-7938 (2004).
37. Xiao, F., Nicholson, C., Hrabe, J. & Hrabetová, S. Diffusion of flexible random-coil dextran polymers measured in anisotropic brain extracellular space by integrative optical imaging. *Biophys J* **95**, 1382-1392 (2008).
38. Tønnesen, J., Inavalli, V. & Nägerl, U.V. Super-Resolution Imaging of the Extracellular Space in Living Brain Tissue. *Cell* **172**, 1108-1121.e1115 (2018).
39. Kuner, T. & Augustine, G.J. A genetically encoded ratiometric indicator for chloride: capturing chloride transients in cultured hippocampal neurons. *Neuron* **27**, 447-459 (2000).
40. Grimley, J.S.*, et al.* Visualization of synaptic inhibition with an optogenetic sensor developed by cell-free protein engineering automation. *Journal of Neuroscience* **33**, 16297-16309 (2013).
41. Marinsky, J.A. An interpretation of the sensitivity of weakly acidic (basic) polyelectrolyte (cross-linked and linear) equilibria to excess neutral salt. *The Journal of Physical Chemistry* **89**, 5294-5302 (1985).

42. Golgi, C. Intomo alla struttura delle cellule nervose. *Boll Soc Med-Chir Pavia* **1**, 1-14 (1898).
43. Celio, M.R., Spreafico, R., De Biasi, S. & Vitellaro-Zuccarello, L. Perineuronal nets: past and present. *Trends Neurosci* **21**, 510-515 (1998).
44. Voipio, J.*, et al.* Comment on "Local impermeant anions establish the neuronal chloride concentration". *Science* **345**, 1130 (2014).
45. Glykys, J.*, et al.* Response to comments on "Local impermeant anions establish the neuronal chloride concentration". *Science* **345**, 1130 (2014).
46. Fuse, T. & Toshiya, S. Preparation and properties of agar sulfates. *Agricultural and biological chemistry* **39**, 119--126 (1975).
47. Gregor, H.P. Gibbs-Donnan equilibria in ion exchange resin systems. *Journal of the American Chemical Society* **73**, 642-650 (1951).
48. Frantz, C., Stewart, K.M. & Weaver, V.M. The extracellular matrix at a glance. *J Cell Sci* **123**, 4195-4200 (2010).
49. Biwersi, J., Farah, N., Wang, Y.-X., Ketcham, R. & Verkman, A. Synthesis of cell-impermeable Cl- sensitive fluorescent indicators with improved sensitivity and optical properties. *American Journal of Physiology-Cell Physiology* **262**, C243-C250 (1992).
50. Düsterwald, K.M.*, et al.* Biophysical models reveal the relative importance of transporter proteins and impermeant anions in chloride homeostasis. *Elife* **7** (2018).
51. Doyon, N., Vinay, L., Prescott, S.A. & De Koninck, Y. Chloride regulation: a dynamic equilibrium crucial for synaptic inhibition. *Neuron* **89**, 1157-1172 (2016).
52. Brumback, A.C. & Staley, K.J. Thermodynamic regulation of NKCC1-mediated Cl- cotransport underlies plasticity of GABA(A) signaling in neonatal neurons. *J Neurosci* **28**, 1301-1312 (2008).
53. Lewin, N., Aksay, E. & Clancy, C.E. Computational modeling reveals dendritic origins of GABA(A)-mediated excitation in CA1 pyramidal neurons. *PLoS One* **7**, e47250 (2012).
54. Beckstein, O. & Naughton, F. General principles of secondary active transporter function. *Biophys Rev (Melville)* **3**, 011307 (2022).
55. Staley, K.J. & Proctor, W.R. Modulation of mammalian dendritic GABA(A) receptor function by the kinetics of Cl- and HCO3- transport. *J Physiol* **519 Pt 3**, 693-712 (1999).
56. Jedlicka, P., Deller, T., Gutkin, B.S. & Backus, K.H. Activity-dependent intracellular chloride accumulation and diffusion controls GABA(A) receptor-mediated synaptic transmission. *Hippocampus* **21**, 885-898 (2011).
57. Barker, J.L. & Ransom, B.R. Amino acid pharmacology of mammalian central neurones grown in tissue culture. *J Physiol* **280**, 331-354 (1978).
58. Alger, B.E. & Nicoll, R.A. Pharmacological evidence for two kinds of GABA receptor on rat hippocampal pyramidal cells studied in vitro. *J Physiol* **328**, 125-141 (1982).
59. Huguenard, J.R. & Alger, B.E. Whole-cell voltage-clamp study of the fading of GABA-activated currents in acutely dissociated hippocampal neurons. *J Neurophysiol* **56**, 1-18 (1986).
60. Staley, K.J., Soldo, B.L. & Proctor, W.R. Ionic mechanisms of neuronal excitation by inhibitory GABAA receptors. *Science* **269**, 977-981 (1995).
61. Rasmussen, M.K., Mestre, H. & Nedergaard, M. Fluid transport in the brain. *Physiol Rev* **102**, 1025-1151 (2022).
62. Staley, K. Ionic mechanisms of ictogenic disinhibition. in *Jasper's Basic Mechanisms of the Epilepsies* (In Press, 2023).
63. Li, M., Toombes, G.E., Silberberg, S.D. & Swartz, K.J. Physical basis of apparent pore dilation of ATP-activated P2X receptor channels. *Nat Neurosci* **18**, 1577-1583 (2015).
64. Celio, M.R. & Blümcke, I. Perineuronal nets--a specialized form of extracellular matrix in the adult nervous system. *Brain Res Brain Res Rev* **19**, 128-145 (1994).

65. Syková, E. & Nicholson, C. Diffusion in brain extracellular space. *Physiol Rev* **88**, 1277-1340 (2008).
66. Tsien, R.Y. Very long-term memories may be stored in the pattern of holes in the perineuronal net. *Proc Natl Acad Sci U S A* **110**, 12456-12461 (2013).
67. Margolis, R.K. & Margolis, R.U. The turnover of hexosamine and sialic acid in glycoproteins and mucopolysaccharides of brain. *Biochim Biophys Acta* **304**, 413-420 (1973).
68. Héron, B.*, et al.* Incidence and natural history of mucopolysaccharidosis type III in France and comparison with United Kingdom and Greece. *Am J Med Genet A* **155a**, 58-68 (2011).
69. Seo, J.H., Okuyama, T., Shapiro, E., Fukuhara, Y. & Kosuga, M. Natural history of cognitive development in neuronopathic mucopolysaccharidosis type II (Hunter syndrome): Contribution of genotype to cognitive developmental course. *Mol Genet Metab Rep* **24**, 100630 (2020).
70. Hampe, C.S.*, et al.* Mucopolysaccharidosis Type I: A Review of the Natural History and Molecular Pathology. *Cells* **9** (2020).
71. Sidharthan, N.P., Minchin, R.F. & Butcher, N.J. Cytosolic sulfotransferase 1A3 is induced by dopamine and protects neuronal cells from dopamine toxicity: role of D1 receptor-N-methyl-D-aspartate receptor coupling. *J Biol Chem* **288**, 34364-34374 (2013).
72. Glykys, J.*, et al.* Chloride dysregulation, seizures, and cerebral edema: a relationship with therapeutic potential. *Trends in neurosciences* **40**, 276-294 (2017).
73. Zhang, S.*, et al.* Distinct roles for metalloproteinases during traumatic brain injury. *Neurochem Int* **96**, 46-55 (2016).
74. Jha, R.M., Kochanek, P.M. & Simard, J.M. Pathophysiology and treatment of cerebral edema in traumatic brain injury. *Neuropharmacology* **145**, 230-246 (2019).
75. Cohen, I., Navarro, V., Clemenceau, S., Baulac, M. & Miles, R. On the origin of interictal activity in human temporal lobe epilepsy in vitro. *Science* **298**, 1418-1421 (2002).
76. Karlócai, M.R.*, et al.* Enhanced expression of potassium-chloride cotransporter KCC2 in human temporal lobe epilepsy. *Brain Struct Funct* **221**, 3601-3615 (2016).
77. González, M.I. Regulation of the cell surface expression of chloride transporters during epileptogenesis. *Neurosci Lett* **628**, 213-218 (2016).
78. Thom, M. Review: Hippocampal sclerosis in epilepsy: a neuropathology review. *Neuropathol Appl Neurobiol* **40**, 520-543 (2014).
79. Roll, L. & Faissner, A. Influence of the extracellular matrix on endogenous and transplanted stem cells after brain damage. *Front Cell Neurosci* **8**, 219 (2014).
80. Song, I. & Dityatev, A. Crosstalk between glia, extracellular matrix and neurons. *Brain Res Bull* **136**, 101-108 (2018).
81. Verkman, A.S. Development and biological applications of chloride-sensitive fluorescent indicators. *Am J Physiol* **259**, C375-388 (1990).
82. Torres, P.B.*, et al.* Determination of sulfate in algal polysaccharide samples: a step-by-step protocol using microplate reader. *Ocean and Coastal Research* **69** (2021).
83. Florence, T.M. & J., F.Y. Spectrophotometric determination of chloride at the parts-per-billion level by the mercury(II) thiocyanate method. *Analytica chimica acta* **54**, 373--377 (1971).
84. Gehlen, M.H. The centenary of the Stern-Volmer equation of fluorescence quenching: From the single line plot to the SV quenching map. *Journal of photochemistry and photobiology. C, Photochemistry reviews* **42**, 100338 (2020).
85. Berdichevsky, Y.*, et al.* Staged anticonvulsant screening for chronic epilepsy. *Ann Clin Transl Neurol* **3**, 908-923 (2016).
86. Stoppini, L., Buchs, P.A. & Muller, D. A simple method for organotypic cultures of nervous tissue. *J Neurosci Methods* **37**, 173-182 (1991).

87. Che, A. & De Marco García, N.V. An in vivo Calcium Imaging Approach for the Identification of Cell-Type Specific Patterns in the Developing Cortex. *Front Neural Circuits* **15**, 747724 (2021).